Miriam Meyer, BSc

Nuclear Wave Packet Dynamics of Indium Dimers inside Superfluid Helium Nanodroplets

MASTER'S THESIS

to achieve the university degree of

Diplom-Ingenieur

Master's degree programme: Technical Physics

submitted to

Graz University of Technology

Supervisor:
Assoc.-Prof. Dipl.-Ing. Dr. Markus Koch

Institute of Experimental Physics

Graz, October 2018

Affidavit

I declare that I have authored this thesis independently, that I have not used other than the declared sources/resources, and that I have explicitly indicated all material which has been quoted either literally or by content from the sources used. The text document uploaded to TUGRAZonline is identical to the present master‘s thesis.

Graz, _____ _____

Date Signature

Eidesstattliche Erklärung

Ich erkläre an Eides statt, dass ich die vorliegende Arbeit selbstständig verfasst, andere als die angegebenen Quellen/Hilfsmittel nicht benutzt, und die den benutzten Quellen wörtlich und inhaltlich entnommenen Stellen als solche kenntlich gemacht habe. Das in TUGRAZonline hochgeladene Textdokument ist mit der vorliegenden Diplombarbeit identisch

Graz, am _____ _____

Datum Unterschrift

Abstract

Superfluid helium nanodroplets (He_N), which have been used for decades to synthesise and investigate weakly bound molecules, represent a novel sample preparation technique to study ultrafast dynamics in previously inaccessible systems. In this thesis first femtosecond time-resolved investigations of molecules located inside He_N are presented.

Coherent molecular dynamics of indium dimers (In_2) were examined with femtosecond pump-probe spectroscopy, applying photoelectron and photoion detection. Inside He_N, In_2 resides within a solvation shell bubble. As for In atoms (B. Thaler et al., Nature Communications 9 (2018), p. 4006), photoexcitation leads to expansion of the helium solvation shell within 600 fs and ejection of the dimers from the droplet within about 100 ps. In addition to this dopant-helium interaction, pronounced wave packet (WP) dynamics of In_2 were observed immediately after photoexcitation as well as after ejection from the droplet (WP revivals). These observations show that coherence is at least partially conserved during the interaction of the dopant molecule with its helium surrounding, paving the way for femtochemistry experiments inside He_N.

In the course of this thesis, the solvation dynamics of In_2 inside superfluid He_N were examined. Subsequently, coherent WP dynamics of In_2 in He_N were investigated using various excitation energies, He droplet sizes and probe pulse parameters. In-He_n ($n = 1...28$) exciplex formation was observed, where the exciplex yield also exhibited oscillations. WP dynamics were analysed using sliding window Fourier transformation. Also, it was investigated whether several In atoms reside in separate solvation bubbles within one He_N that collapse upon photoexcitation and form an In aggregate. Finally, to gain a deeper insight into WP dynamics the temporal evolution of a WP in a Morse potential was simulated using Matlab.

The following publications have emerged from this work:

- **Femtosecond solvation dynamics of indium dimers inside superfluid helium nanodroplets**
  M. Meyer, B. Thaler, P. Heim, M. Koch. EPJ Web of Conferences, accepted 2018
- **Coherent wavepacket dynamics inside a quantum solvent**
  B. Thaler, M. Meyer, P, Heim, M. Koch. In preparation 2018

Kurzfassung

Superfluide Helium Nanotröpfchen (He_N), die jahrzehntelang zur Synthetisierung schwach gebundener Moleküle verwendet wurden, repräsentieren eine neuartige Methode Proben zu präparieren um ultraschnelle Dynamiken in vormals unzugänglichen Systemen zu beobachten. In dieser Diplomarbeit werden erste zeitaufgelöste Untersuchungen von Molekülen in He_N mit femtosekunden Zeitauflösung präsentiert.

Kohärente Moleküldynamiken von Indium Dimeren (In_2) wurden mittels Femtosekunden-Pump-Probe-Spektroskopie, durch Messung von Photoelektronen und Photoionen, untersucht. In_2 befindet sich innerhalb der He_N in einer Solvationshülle. Wie für Indium Atome (B. Thaler et al., Nature Communications 9 (2018), p. 4006), führt Photoanregung zur Expansion der Solvationshülle innerhalb von 600 fs und Auswurf des Dimers aus dem Nanotröpchen innerhalb von etwa 100 ps. Zusätzlich zur Interaktion zwischen dem Dopanden und dem Helium wurden ausgeprägte Wellenpaket(WP)-Dynamiken des In_2 unmittelbar nach der Photoanregung, ebenso wie nach Auswurf aus dem Tröpfchen (WP Revival), beobachtet. Diese Ergebnisse zeigen, dass Kohärenz während der Interaktion des Dopanden mit der Heliumumgebung zumindest teilweise erhalten bleibt, was den Weg für Femtochemie Experimente in He_N ebnet.

Im Zuge dieser Diplomarbeit wurden Lösungsdynamiken von In_2 in superfluiden He_N, und daraufhin kohärente WP-Dynamiken mit unterschiedlichen Anregungsenergien, He Tröpfchengrößen und Probepulsparametern untersucht. In-He_n ($n = 1...28$) Exciplexe wurden beobachtet, deren Signal auch Oszillationen zeigte. Die WP-Dynamiken wurden mit Hilfe von Gleitener-Fenster-Fourier-Transformation analysiert. Außerdem wurde untersucht, ob sich mehrere In Atome in separaten Solvationshüllen innerhalb eines He_N befinden, welche nach Photoanregung kollabieren und sich ein In-Aggregat bildet. Schlussendlich wurde, um ein besseres Verständnis von WP-Dynamiken zu erlangen, die zeitliche Entwicklung eines WPs in einem Morsepotential mit Hilfe von Matlab simuliert.

Die folgenden Publikationen sind im Rahmen dieser Arbeit entstanden:

- **Femtosecond solvation dynamics of indium dimers inside superfluid helium nanodroplets**
  M. Meyer, B. Thaler, P. Heim, M. Koch. EPJ Web of Conferences, accepted 2018
- **Coherent wavepacket dynamics inside a quantum solvent**
  B. Thaler, M. Meyer, P, Heim, M. Koch. In preparation 2018

Contents

1 Introduction **1**

1.1 Vibrational Wave Packets 2

1.1.1 Vibrational Wave Packets in Liquids and Solids 4

1.1.2 Indium Dimer 7

2 Experimental **9**

2.1 Experimental Setup 9

2.2 Pickup Current Source Emergency Shutdown System 11

2.2.1 Pressure Control 11

2.2.2 Flow Control 12

2.3 TOF Energy Resolution 13

3 Results **15**

3.1 Solvation Dynamics of In_2 inside Superfluid Helium Nanodroplets 15

3.1.1 Introduction 15

3.1.2 Method 16

3.1.3 Results and Discussion 16

3.2 Nuclear Wave Packet Oscillation 18

3.3 Excitation at the 345 nm Band 19

3.3.1 Excitation at 345 nm 19

3.3.2 Compare results for 1 mm BBO to 5 mm LBO crystal 29

3.3.3 Excitation at 333 nm 30

3.3.4 Excitation at 327 nm 34

3.4 Excitation at the 365 nm Band 35

3.4.1 Excitation at 360 nm 35

3.4.2 Excitation at 365 nm 37

3.4.3 Compare WP oscillations for excitation at 345 nm and 364 nm . . . 40

3.5 Investigate Possible Foam Collapse 41
3.6 Exciplex Formation 43
3.6.1 Exciplex oscillation 46

4 The Wave Packet in a Morse Potential 49
4.1 The Morse Potential and its Vibrational Eigenstates 49
4.2 Temporal Evolution of a Vibrational Wave Packet 52

5 Outlook 59

6 Appendix 63
A Sliding Window Fourier Transformation 63
A.1 Introduction to SWFT 63
A.2 SWFT Matlab Code 67
B WP Simulation 68

Bibliography 77

Danksagung 83

CHAPTER 1

Introduction

Superfluid helium nanodroplets (He_N) have been used for several decades to synthesize otherwise inaccessible molecular systems [1, 2] like weakly bound molecules or core shell clusters. They also can be used as nanoscopic cryostats at a temperature of 0.4 K [3] to isolate atoms or molecules. Furthermore, He_N represent a novel sample preparation technique to perform spectroscopic studies on those unstable species [4, 5].
Studying ultrafast processes in molecules is of high interest, because it helps to investigate chemical reactions and fundamental biological processes on their natural timescale. The groundstone for femtochemistry was laid by Ahmed Zewail, who was awarded the Nobel Prize for Chemistry in 1999 [6].
In the research presented here the unique possibilities of He_N as a sample preparation technique are combined with ultrafast laser spectroscopy as investigation method. So far, studies have been restricted to pure He_N [7] and alkali atoms residing on the droplet surface [8, 9]. Here, dopants that are fully immersed inside the droplets are investigated. In order to fully understand the complex interaction of a photoexcited dopant with the superfluid helium surrounding, experiments were at first conducted at the simplest system, a single immersed atom [10]. It has been shown that it is possible to observe electronic and nuclear dynamics of a dopant that is fully immersed in He_N. Photoelectrons have proven to be a well suited observable for the dynamics. It has been shown that the solvation shell, in which indium (In) resides, expands upon photoexcitation, corresponding to the enlarged radial distribution of the valence electron, within 600 fs. The impulsive expansion triggers an oscillation of the solvation bubble with a period of approximately 30 ps. The In atom was also found to be ejected from the droplet upon photoexcitation.

After this proof of concept the next logical step was to move on to investigate the simplest molecule, a dimer. In the course of this thesis coherent molecular dynamics of molecules immersed in He_N have been successfully measured for the very first time. The next few pages will give an introduction to nuclear wave packet (WP) dynamics.

1.1 Vibrational Wave Packets

A vibrational WP consists of a coherent superposition of vibrational molecular states. It can be created by photoexcitation with a short light pulse of a certain spectral band width. Figure 1.1 depicts a schematic representation of the excitation and probing mechanism. Initially, the molecule is prepared in its electronic and vibrational ground state. When the potential energy curve of the electronically excited state has its minimum at a larger internuclear distance than the ground state, the WP will be excited by the pump laser pulse (indicated as a black upward arrow in the figure) at the classical inner turning point of the excited state potential. The electronic excitation process happens so fast, that there is not enough time for the atomic nuclei to relax into their equilibrium distance (Born-Oppenheimer approximation). Therefore, at the inner turning point there is a larger Franck-Condon overlap between the vibrational wavefunction of the ground and the excited state.

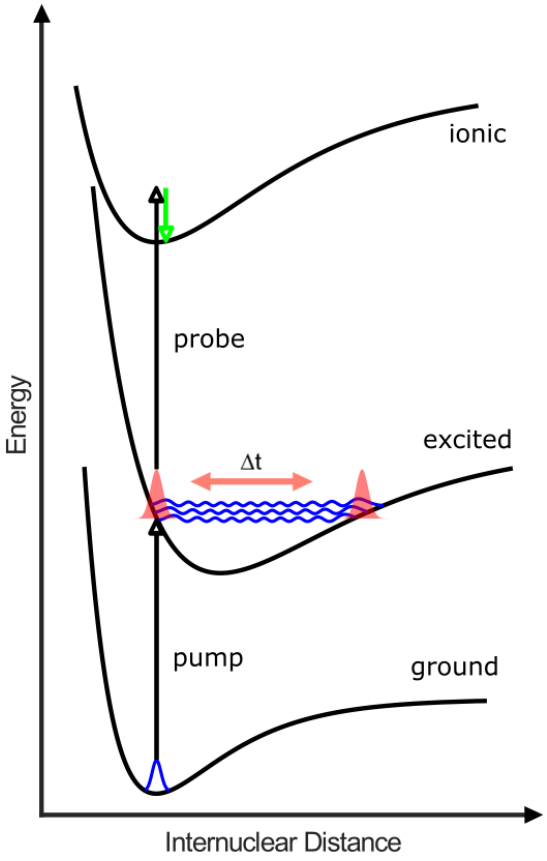

Figure 1.1: Schematic representation of the WP excitation and probing mechanism: A pump laser pulse (lower black upward arrow) coherently couples several vibrational states in an electronically excited state. The temporal evolution of the wave packet is probed with a second time delayed laser pulse (probe pulse, upper black upward arrow). The green arrow represents the kinetic energy of the ejected electron.

A coherent superposition of states means that a certain phase relation is established between the vibrational states during the excitation process. For isolated

diatomic molecules in gas phase, that do not interact with any other molecules, the phase relation is maintained throughout the evolution of the WP. For a relatively short time after its creation, the WP is localised and oscillates back and forth from the classical inner to the outer turning point of the potential (see figure 1.1 in the excited state).
However, because the different states in an anharmonic potential are not equidistantly spaced, the vibrational states evolve with different phase velocities. For more information see also chapter 4. The higher lying ('blue') states evolve with a smaller phase velocity than the lower lying ('red') states and the wave packet disperses. Since the phase relation is maintained, the different vibrational states will catch up with each other again after the so called 'revival time', which can be calculated for a Morse potential with the following formula [11]:

$$T_{rev} = \frac{2\pi}{\omega_e x_e}, \tag{1.1}$$

$$\text{with } x_e = \frac{\hbar\omega_e}{4D_e}.$$

$\omega_e x_e$ represents the anharmonicity of a Morse potential. It can be seen that a large anharmonicity results in a short revival time and vice versa. At the revival time all vibrational states are in phase again and the WP shows the same sharply localised feature as immediately after its creation.
Probing of the WP occurs with a second time delayed probe laser pulse, again indicated by a black upward arrow in figure 1.1. The energy of the probe pulse has to be chosen in such a way that it exceeds the potential energy difference between the excited and the ionic state. This resonance condition will be different at the inner and the outer turning point, which implies that by choosing a certain probe laser wavelength the internuclear distance at which the WP is probed can be determined. The internuclear separation, at which the resonance condition is fulfilled, is called the 'Franck-Condon window' [12]. As the WP oscillates across the potential, it moves in and out of the Franck-Condon window and an increased, respectively decreased, photoelectron and -ion yield is obtained. When the WP has dispersed, the probability of presence is approximately the same across the whole potential energy curve and there will be no periodic fluctuation in the measured signal. When the WP has reformed after the revival time, the same oscillating electron or ion signal will be measured (see figure 1.3, top). The green downward arrow in figure 1.1 represents the kinetic energy of the ejected photoelectrons.

At the revival time T_{rev} all the vibrational wave functions of which the WP consists are in phase again and all wave functions have the same phase they had at the time of the excitation. This is called a 'full revival'. At the so called half revival time $T_{rev}/2$ also all wave functions are in phase, however the phase of all wave functions is shifted 180° with

respect to their initial phases. Because the probe pulse probes the probability of presence, the electron- and ion yield will look exactly the same as at the time of a full revival.
There are also so called fractional revivals. These occur when subgroups of the involved vibrational wave functions are in phase. At a quarter revival, which occurs at $T_{rev}/4$, two subgroups are in phase. This corresponds to two localised features on the potential curve that both oscillate across the potential. This leads to the measurement of two times the frequency of the half and full revival. At $T_{rev}/6$ three subgroups are in phase. A $1/6^{\text{th}}$ revival can be observed, oscillating at three times the fundamental frequency. The number of fractional revivals is limited by the limited number of coherent vibrational states. For example a $1/6^{\text{th}}$ revival requires at least four states that are still coupled coherently [13].

Vibrational wave packets in gas phase have been subject to intensive experimental (see e.g. references [14, 15, 16]), as well as theoretical [17], studies.
An interesting experiment was conducted by Liu et al. [18], who investigated the coherence of vibrational WPs in I_2 in the transition from a gas phase to a liquid surrounding, by increasing the pressure of a surrounding noble gas from 0 bar to several thousand bar.

1.1.1 Vibrational Wave Packets in Liquids and Solids

When the molecule, in which a WP is excited, is not isolated any more, but rather surrounded by a liquid or solid, there will be interaction between the molecule and the surrounding through elastic as well as inelastic scattering. The phase relation, which has been imprinted on the vibrational states upon excitation, can get lost during a scattering event. Figure 1.2 shows schematically what happens to the WP upon elastic (left) and inelastic (right) collision with the surrounding.

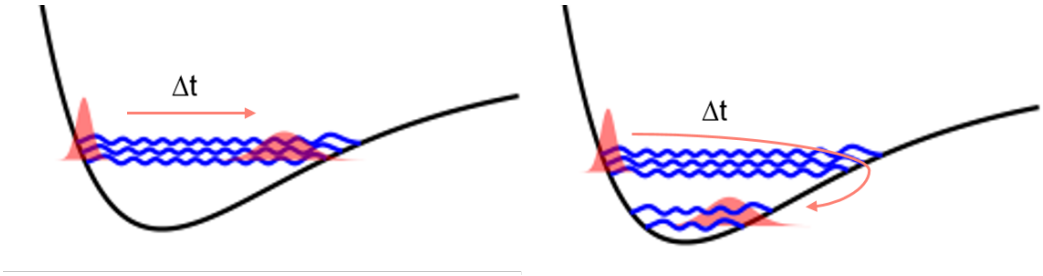

Figure 1.2: Schematic representation of the dephasing and dissipation process of a vibrational WP. Left: The phase relation between different vibrational states can be lost due to elastic scattering with surrounding molecules. This is called decoherence. Right: In an inelastic scattering event the phase relation can be lost and energy is dissipated to the surrounding. The WP moves to lower vibrational states.

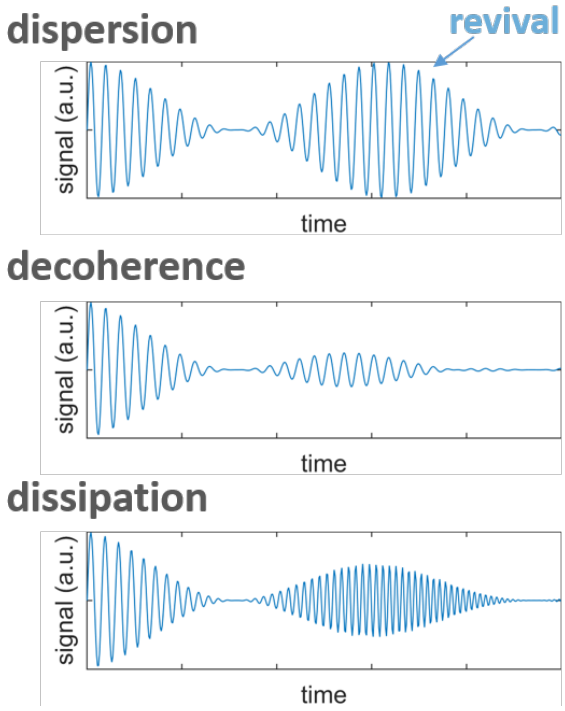

Figure 1.3: Schematic representation of the revival of a vibrational WP. If coherence is fully conserved, the amplitude of the oscillating signal at the half and full revival is the same as immediately after creation of the WP, there is only dispersion (top image). If coherence is lost during elastic scattering events with surrounding atoms or molecules the revival will show a decreased oscillation amplitude, there is decoherence (middle image). When there is decoherence as well as dissipation due to inelastic scattering events with the surrounding, the revival will show a decreased amplitude as well as an increased oscillation frequency (bottom image). Note that when there is decoherence, the amplitude of the revival reaches a maximum earlier, than without decoherence. This is due to the multiplication of the oscillating signal with an exponential decay, which represents the dephasing. With kind permission by Bernhard Thaler.

In an elastic collision, phase information will be lost, but the molecule will transfer no energy to the surrounding. The WP stays at the same height within the potential energy curve, but it suffers irreversible broadening. This effect is synonymously called decoherence or dephasing. When the revival time is reached, the WP will not be as sharply focused as it had been immediately after its creation. This also means that the amplitude of the oscillating electron or ion signal will be smaller (see figure 1.3, middle).

During an inelastic scattering process, there will be a loss of phase relation and also the molecule dissipates energy to its surrounding, so there is decoherence as well as dissipation (see figure 1.3, bottom). Again, the amplitude of the oscillating signal decreases due to decoherence. Dissipation causes an increase of oscillatory frequency, because the lower lying vibrational states are energetically more widely spaced in an anharmonic potential.

It is desirable to understand the influence of surrounding atoms and molecules on vibrational coherence, because a better understanding will open up new possibilities concerning the coherent control of chemical reactions. To characterise the decoherence properties of solvent molecules or atoms, coherent WP dynamics of molecules were investigated in solid rare gas matrices, attached to He_N and in solution.

Coherent dynamics of ClF, Cl_2, Br_2 and I_2 in solid Kr and Ar matrices are summarised in [13]. Decoherence times were determined by systematically varying the chirp of the excitation laser pulse. It was also shown that the shape of the anharmonic potential can be experimentally measured by a systematic variation of pump and probe wavelengths. Coherence times were found to be larger compared to molecules in a liquid or high pressure gas phase surrounding. In [19] "Vibrational coherence of I_2 in solid Kr" was measured up to 100 ps after excitation. Due to the long coherence time the frequency spectrum has very high resolution and peaks in the spectrum can be assigned to the coupling between different vibrational states. The same system was investigated in reference [20], where it was shown that vibrational coherence can still be observed after a strongly inelastic scattering event of the I_2 with the surrounding Kr atoms and that even after an electronic transition, vibrational coherence can still be observed in the final state.

To investigate the vibrational coherence of molecules attached to He_N exclusively alkalis were chosen, because they were known to reside on the droplet surface and therefore a weak perturbation by the helium was expected. Experimental investigations were performed on Na_2 [21], Rb_2 [22, 23], K_2 [24, 25]. Theoretical studies concerning the influence of He_N on the vibrational coherence of attached molecules can be found in [26, 27, 28]. Also rotational WPs of molecules attached to He_N have been investigated [29, 30, 31, 32]. Schmidt et al. had tried to measure coherent molecular dynamics of LiI immersed in He_N [33], which, however, was not successful. The observables in the experiment were the total photoelectron and Li^+-yield. The coherent WP dynamics measured in gas phase could not be observed for LiI embedded in He_N.

It was found that upon photoexcitation of molecules attached to or immersed in He_N exciplex formation can occur. This was investigated for K [34, 35] and Rb [36, 37, 38]. Also photoinduced cluster formation of Mg atoms was observed. The Mg atoms initially resided in separate He solvation shells, which collapsed upon photoexcitation [39, 40].

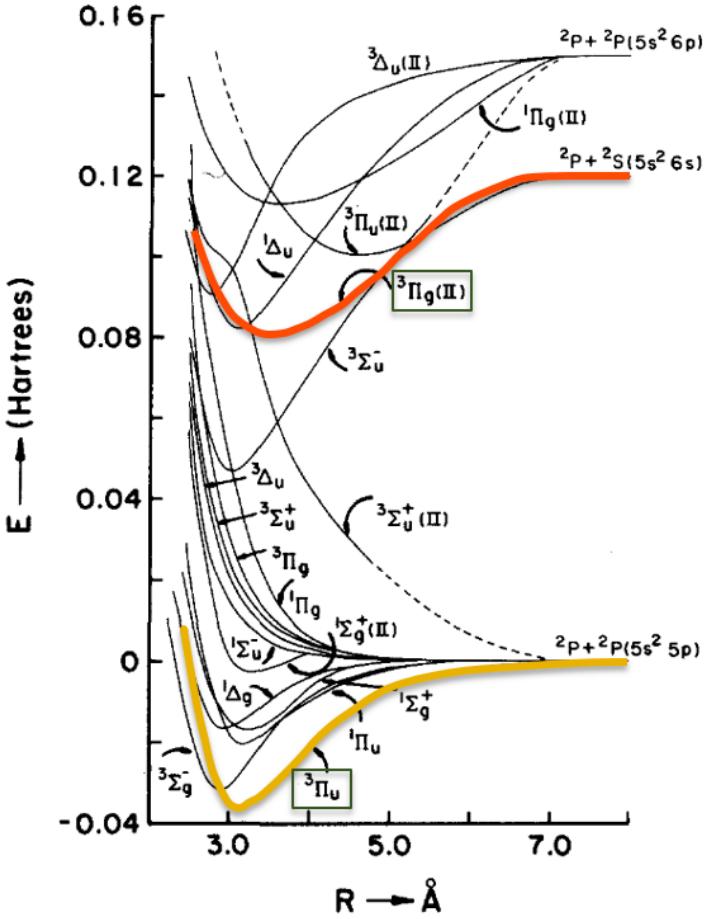

Figure 1.4: Calculated potential energy curves of In_2 from reference [42]. The yellow curve marks the electronic ground state. The red curve highlights the state that is excited in the experiment.

1.1.2 Indium Dimer

The molecule under investigation in this thesis is the indium dimer (In_2). Because this molecule does not naturally form, it has to be prepared artificially for example in a cryogenic matrix in order to be investigated experimentally [41]. The potential energy curves for In_2 have also been calculated [42, 43]. For the simulation in chapter 4 the fitted Morse potential parameters were taken from reference [42]. The values are listed in table 4.1.

CHAPTER 2

Experimental

In this chapter an overview of the experimental setup is given. A more detailed description can be found in the masters's theses of Sascha Ranftl [44], Stefan Cesnik [45] and Bernhard Thaler [46]. The installation of an emergency shut down mechanism for the current source that provides the pick up current is documented here as well as a further optimisation of the energy resolution of the time-of-flight (TOF) spectrometer.

2.1 Experimental Setup

The system that was to be investigated in the course of this thesis, In_2 doped superfluid He nanodroplets, was studied using a pump-probe setup with femtosecond time resolution. The experimental setup is schematically shown in figure 2.1.
The laser pulses are generated with a commercially available titanium-sapphire laser system (Coherent Vitara oscillator, Legend Elite Duo amplifier). The obtained pulses have 25 fs duration with 3 kHz repetition rate, an average power of 13 W and a center wavelength of 800 nm. The pulses are split into two beams, the pump and the probe beam, with a beam splitter (BS in figure 2.1). The pump beam is frequency upconverted in an optical parametric amplifier (OPA, Coherent OPerA Solo) to the desired excitation wavelength (327 nm to 365 nm). To compensate the positive chirp that has accumulated by passing through the OPA, the beam passes through a prism compressor, a wire grid polariser (both not shown in figure 2.1) and is then focussed into the measurement chamber. The probe beam is guided across a translational delay stage, to provide a variable time delay between the pump and the probe pulse. The probe pulse is then frequency upconverted by

second harmonic generation (SHG) using either a 1 mm thick beta barium borate (BBO) or a 5 mm lithium triborate (LBO) crystal, to about 406 nm and subsequently focussed into the measurement chamber.

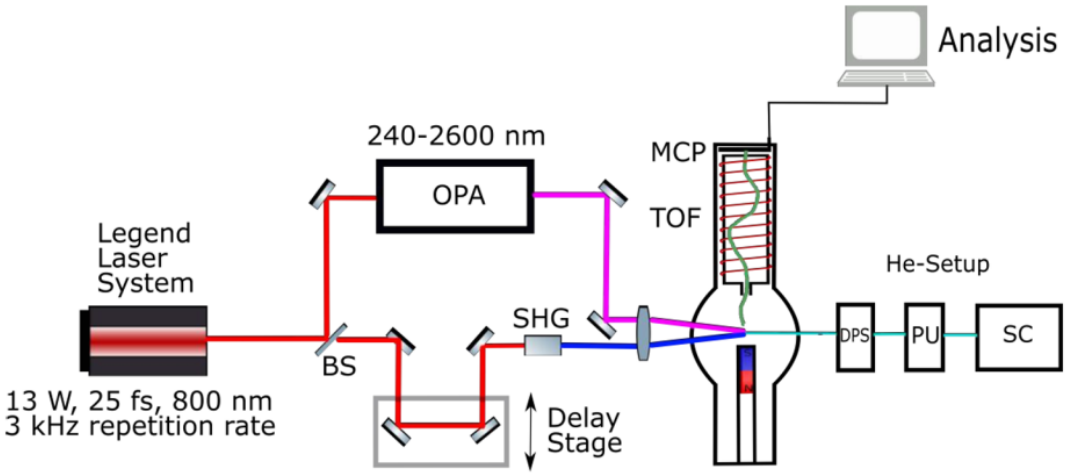

Figure 2.1: Schematic representation of the experimental setup. BS: beam splitter, OPA: optical parametric amplifier, SHG: second harmonic generation, TOF: time-of-flight spectrometer, MCP: microchannel plate, DPS: differential pumping stage, PU: pick up chamber, SC: source chamber.

The beam of superfluid He nanodroplets is generated in a supersonic expansion. High purity He at 40 bar stagnation pressure is expanded through a precooled nozzle of 5 µm diameter. The nozzle was operated at a temperature of 18 K, 15 K and 13 K to produce He droplets with a mean number of $\bar{N} = 4800$, $\bar{N} = 8000$ and $\bar{N} = 13000$ He atoms, respectively. The He beam passes through a resistively heated pickup cell within the pickup chamber (PU), where the droplets pick up on average two In atoms. The beam then passes through a differential pumping stage (DPS) and finally intersects with the laser beams in the measurement chamber.
The pump pulse excites the dopant within the He droplet and the time delayed probe pulse ionises it. The photoelectrons and photoions are detected with a magnetic bottle type TOF spectrometer. While the heavy ions are pushed towards the detector with a high voltage (2 kV) applied to the repeller, the light electrons are guided toward the detector by the magnetic field. A small positive voltage can also be applied to the repeller when detecting photoelectrons in order to increase the resolution of the spectrometer. The photoelectrons and -ions are detected with a microchannel plate (MCP). The measured signal (photoelectron kinetic energy and ion charge-to-mass ratio) is digitalised and analysed on a computer.
For a more detailed description of the experimental setup see references [45] and [44]. For information on data acquisition and data analysis see reference [46].

2.2 Pickup Current Source Emergency Shutdown System

A lot of tools have been installed in the experimental setup to enable automated measurements. Measurement routines written in Matlab control the delay stage, shutters to block and unblock laser beams, start data acquisition etc. Because this means that measurements can be performed while the laboratory is unattended by any personnel, some security systems had to be installed to ensure the shutdown of possibly hazardous devices in case something goes wrong.

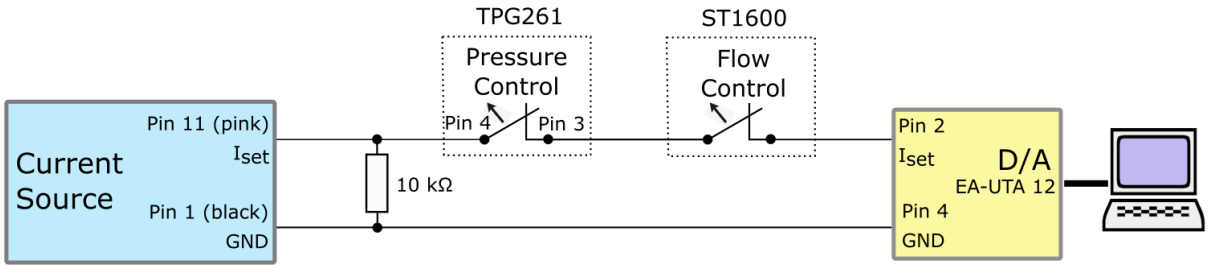

Figure 2.2: Schematic circuit diagram for current source security system

A new emergency shutdown system has been installed for the pickup current current source. The schematic circuit diagram can be seen in figure 2.2 (for pin assignments see reference [44]).
The current for the resistively heated pickup cell can be set digitally via a computer. The signal is converted in a D/A converter device and sets the current value analogously at the current source. The two pins that set the current are connected in series with a pressure control and a flow control unit. The pin that sets the current value analogously at the current source is also connected in parallel to ground (GND) over a 10 kΩ resistor. If either one or both of the control units open a switch, the current is set to zero (ground).

2.2.1 Pressure Control

The pressure in the pickup chamber is measured with a Balzers PBR 260 pressure gauge, which is operated with a TPG 261 controller. A threshold pressure value can be set at the controller. When the pressure rises above that threshold a switch opens. The pin assignment for the pressure control unit is shown in figure 2.3. A description of how to set the value for the threshold pressure can be found in the TPG 261 manual [47].

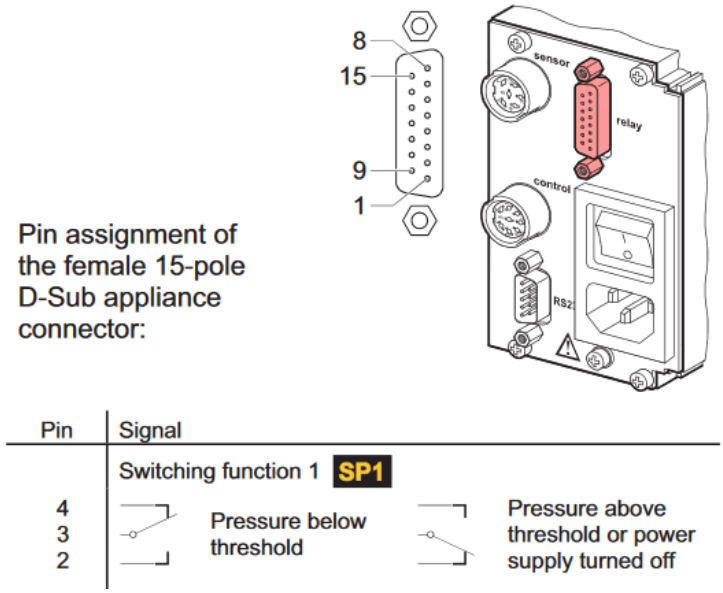

Figure 2.3: Pin assignment for pressure control. The picture was taken from the TPG 261 controller manual [47].

2.2.2 Flow Control

An ST1600 flow sensor by the ifm electronic gmbh was installed to control the water flow through the water cooling system for the pickup cell. The water flow is measured with the sensor shown in figure 2.4. LEDs indicate the status of the water flow sensor. The orange light is on, when the sensor is connected to a supply voltage. Green light indicates that enough water flows through the sensor, while red light indicates an insufficient water flow. The water flow threshold can be set with a small red screw indicated by the blue arrow. The electronic control unit for the flow sensor was built in the electronics workshop of the institute. As long as there is enough water flow, the sensor has an output voltage of 5 V, when the water flow sinks below the threshold, the output voltage is set to zero and the relay opens.

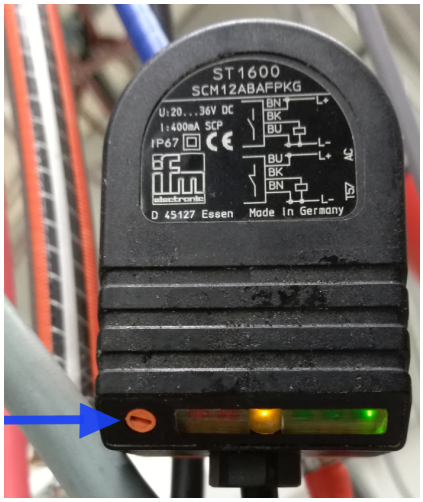

Figure 2.4: Flow control sensor: The orange light means that the sensor is connected to a supply voltage. The green light indicates that there is enough water flow. A red light would indicate insufficient water flow. The blue arrow indicates a red screw where the threshold value for the water flow can be set higher or lower.

2.3 TOF Energy Resolution

Stefan Cesnik characterised the energy resolution of the TOF spectrometer for photoelectron measurements in his masters's thesis [45]. The conclusions that had been drawn from those past measurements were that a low repeller position (several mm below the focus of the laser beam) and a positive repeller voltage to slow down the photoelectrons yield the highest resolution.
Reference [48] also investigated the "Performance of a short 'magnetic bottle' electron spectrometer". In this publication it was found that an acceptance angle of 4π sr of the photoelectrons, which corresponds to a low position of the repeller, decreases the energy resolution by about a factor of 2. This lower energy resolution stems from the photoelectrons that are ejected in the direction opposite of the spectrometer flight tube. It takes some time until these electrons turn around, they have a longer flight time and the measured kinetic energy is smeared out towards lower values. In this publication an acceptance angle of 2π sr is favoured with respect to energy resolution.
However, in a measurement to try to improve the energy resolution of the TOF spectrometer, it was found that moving the repeller slightly (about 2 mm) does not have a large influence on the resolution. The electron spectra are shown in figure 2.5 and the corresponding experimental settings (repeller position and voltage) as well as the half width of the photoelectron peaks are listed in table 2.1. It was confirmed that slowing down the photoelectrons with a positive repeller voltage results in a higher energy resolution.

The energy resolution of 33 meV FWHM obtained at -4.5 mm repeller position and 0.6 V repeller voltage is comparable with the energy resolution determined by Stefan Cesnik [45] (about 30 meV FWHM).

The new scheme for high energy resolution photoelectron measurements:

- Position the repeller at a short distance below the laser focus (about 3 mm to 4 mm).
- Carefully increase the repeller voltage until the photoelectron peak has moved to the lowest possible energy value without losing electron counts.

Table 2.1: TOF Energy Resolution

File	Repeller Position	Repeller Voltage	FWHM
DiffPlotData_21302	−2.5 mm	0.3 V	50 meV
DiffPlotData_21307	−3.5 mm	0.4 V	47 meV
DiffPlotData_21323	−3.5 mm	0.6 V	36 meV
DiffPlotData_21311	−4.5 mm	0.4 V	47 meV
DiffPlotData_21316	−4.5 mm	0.6 V	33 meV
DiffPlotData_21319	−5.5 mm	0.6 V	34 meV

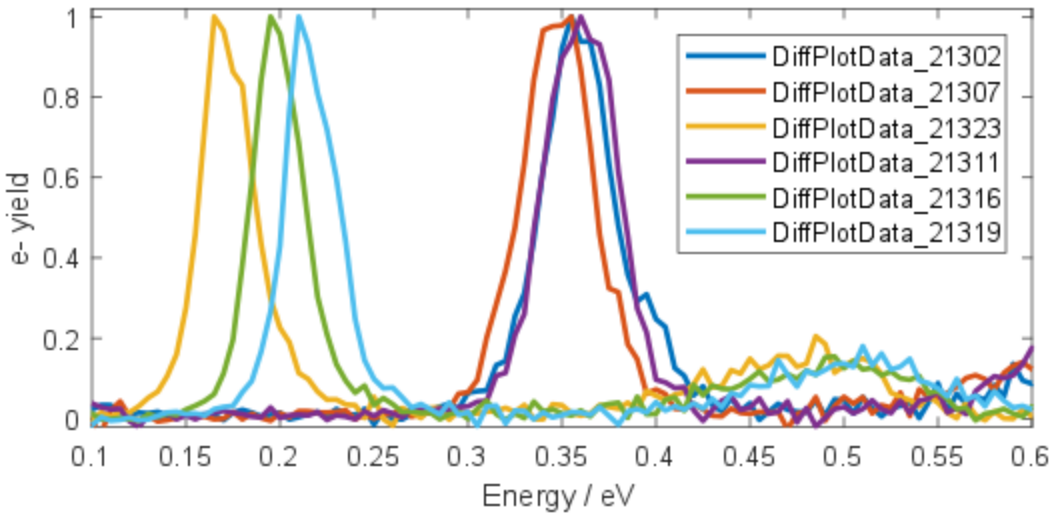

Figure 2.5: The energy resolution of the TOF spectrometer was investigated as function of distance between repeller and laser focus and applied repeller voltage. (Lab.Book: 03.07.2018)

CHAPTER 3

Results

This chapter gives an overview of the experimental results obtained for In_2 in He_N within the course of this thesis. Results on the solvation dynamics are give in section 3.1, the main content of which has been accepted for publication by EPJ Web of Conferences. Additional remarks to the original publication with the title "Femtosecond solvation dynamics of indium dimers inside superfluid helium nanodroplets" [49] have been made in order to give more details. In the following sections the results on coherent vibrational WP dynamics are shown as well as a search for indium trimers (In_3) and In^+He_n exciplex formation.

3.1 Solvation Dynamics of In_2 inside Superfluid Helium Nanodroplets

Section 3.1 has been accepted for publication at EPJ Web of Conferences. The publication has the title "Femtosecond solvation dynamics of indium dimers inside superfluid helium nanodroplets". The authors are M. Meyer, B. Thaler, P. Heim and M. Koch [49].

3.1.1 Introduction

Superfluid helium nanodroplets (He_N) represent a special approach for the synthesis of tailor-made or fragile molecules and clusters. In view of time-resolved spectroscopy, they provide access to novel classes of systems that have eluded ultrafast dynamical studies so far. Pure He_N [7] and surface-located alkali-metals [8] have been subject to femtosecond

experiments. Concerning molecules immersed inside the He_N, the only attempt to observe ultrafast dynamics used the salt molecules sodium- and lithium iodide, which, however, was not successful [33].
Recently, we demonstrated that time-resolved photoelectron (PE) spectroscopy can be used to observe photoinduced dynamics of single atoms that are fully solvated inside the droplet [10]. The PE kinetic energy turned out to be a sensitive observable to follow the temporal evolution of the solvation shell around the photoexcited dopant. Supported by time-dependent density functional theory, we developed the following mechanistic picture: Photoexcitation of a single indium (In) atom inside a He_N leads to expansion of the solvation shell within 600 fs, followed by an oscillation of the bubble with a period of about 30 ps, and, finally, ejection of the In atom from the droplet after about 60 ps.
Here, we investigate the photoexcitation dynamics of the In_2-He_N system, for which we observe solvation dynamics similar to the monomer case, as well as intrinsic In_2 molecular dynamics. In the presented work we concentrate on the former and interpret the corresponding transient signals by comparison to the previous In-He_N results.

3.1.2 Method

As described in detail previously [10, 50], He_N with a mean number of $\bar{N}$=8000 He atoms are generated in a supersonic expansion and doped inside a resistively heated pickup cell with two In atoms per droplet, which form an In_2 molecule. Dynamics of the In_2-He_N system are investigated with a femtosecond pump-probe photoionization experiment with variable time-delay, where the kinetic energy of photoelectrons (PEs) and charge-to-mass ratio of ions are measured with a time-of-flight spectrometer. Pump pulses are obtained from a commercial Ti:sapphire laser system and frequency upconverted by an optical parametric amplifier to a photon energy of 3.59 eV (345 nm) in order to excite the B $^3\Pi_g(\mathrm{II}) \leftarrow$ X $^3\Pi_u$ transition of In_2 inside He_N [50]. Probe pulses are frequency doubled to 3.05 eV (406 nm).

3.1.3 Results and Discussion

Figure 3.1a shows the time evolution of the PE spectrum within the first two picoseconds after photoexcitation. The signal is modulated with a period of about 400 fs, which we ascribe to a nuclear wave packet oscillation of the In_2 molecule. The periodic signal maxima correspond to ionization from the excited B $^3\Pi_g$ (II) state to the cationic ground state of In_2, at a certain nuclear distance of the two In atoms (Condon point) [12]. The In_2 wave packet dynamics will be further analysed in an upcoming publication.

The maxima are energetically shifted by 150 meV from 780 meV to 630 meV within the first picosecond, as indicated by a white line in Figure 3.1a. The line was obtained by an

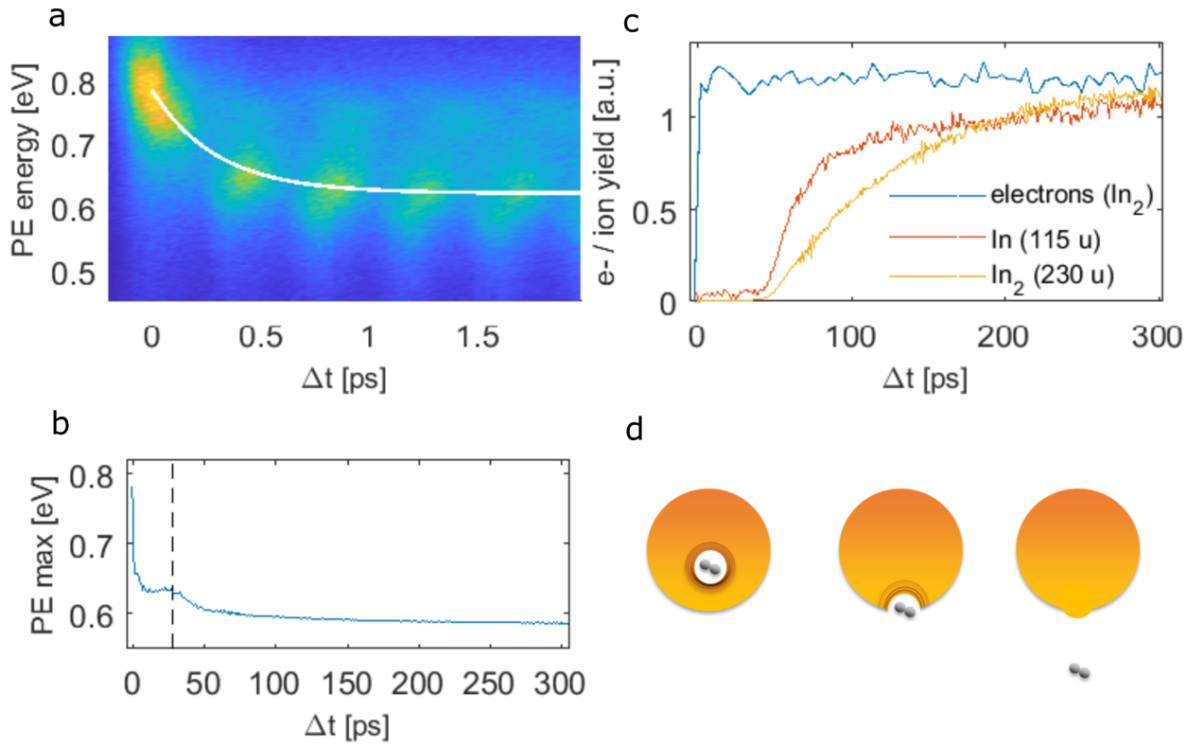

Figure 3.1: Time evolution of the In_2-He_N system after photoexcitation. (a) PE spectrum within the first 2 ps. The white line connects the signal maxima. (b) PE peak position up to 300 ps, as determined by Gaussian fits to the corresponding PE spectra. The dashed line at 28 ps indicates the maximum of the temporal increase in PE energy. (c) Ion yields recorded at the In monomer/dimer masses of 115/230 u for photoexcitation at the monomer/dimer band at 376/345 nm (red/yellow line) and total PE yield integrated over all kinetic energies for excitation at 345 nm (blue line). (d) Sketch of the In_2 ejection process.

exponential fit of the five intensity maxima. This shift is related to the expansion of the He bubble as consequence of the enlargement of the valence electron orbital during photoexcitation [10]. Compared to the In-He_N system, where a shift of 290 meV is observed within 1 ps and 90% peak shift are completed within 500 fs, the shift of the In_2-He_N is smaller (150 meV) and takes longer (90% within 700 fs). Both indicate that the excited state interaction with the He solvation shell is less pronounced for the In dimer compared to the monomer.

The PE peak shift up to 300 ps is shown in Figure 3.1b. After a steep, initial decrease, representing the bubble expansion, the peak position is shifted further towards lower energies with a temporal energetic increase around 28 ps (marked by the dashed line), before it slowly approaches a constant value of ∼590 meV. The impulsive expansion of the solvation shell triggers an oscillation of the He bubble, the first contraction of which leads to the temporal increase in energy. This contraction is observed at the same time

as for the monomer [10]. The decrease after 1 ps of the PE energy represents the ejection process of In_2 from the droplet, as the ionization energy inside the He_N is reduced due to polarization effects [51], compared to that of bare In_2.
Ejection from the He_N is particularly well observed by the transient ion yield. In Figure 3.1c the transient dimer ion yield for photoexcitation at the In_2 band (345 nm, yellow line) is compared to the monomer yield for excitation at the monomer band (376 nm, red line) [50]. Additionally, the total electron yield over time for excitation at 345 nm (blue line) is shown. While the electron signal shows an immediate rise at time-zero and remains constant afterwards, the ion signals both exhibit a delayed onset at 50 ps followed by a faster rise of the monomer within ∼50 ps and a slower dimer rise within ∼200 ps. This shows that In_2 is ejected from the droplet, in consequence of a repulsive, heliophobic excited state, as it is also the case for the In monomer [10]. Due to the cylindrical symmetry of In_2 the repulsive force experienced by the molecule depends on its orientation inside the He_N, which is not the case for the spherically symmetric monomer. This would be a possible explanation for the similar onset time and slower rise of the dimer compared to the monomer.
In conclusion, the photoinduced solvation dynamics of the In_2-He_N system, as sketched in Figure 3.1d, show all three signatures previously observed for In-He_N [10] – bubble expansion, bubble oscillation and dopant ejection. Bubble expansion and ejection proceed more slowly and are less pronounced for In_2 dopants, while the bubble oscillation is surprisingly similar to the atomic case.

3.2 Nuclear Wave Packet Oscillation

The excitation spectrum for atoms and molecules immersed in superfluid He_N shows a blue shift with respect to the gas phase spectrum. For In_2 inside He_N the excitation spectrum is shown in figure 3.2. Two excitation bands can be seen. One is centred around 345 nm, which was assigned to the $^3\Pi_g(II) \leftarrow {}^3\Pi_u$ transition [50] (see figure 1.4). The transition in gas phase occurs at excitation with 362 nm [52]. The second excitation band is centred around 365 nm and is overlapped with an excitation band of the indium monomer immersed in He_N.

Coherent molecular dynamics can be seen in figure 3.1 up to 2 ps time delay. In the following, it will be shown that vibrational coherences in the In_2 molecule can still be seen after the bubble expansion process within the droplet and even after ejection from the superfluid He droplet.
The coherent molecular WP oscillations were investigated at different wavelengths within both excitation bands. Half as well as full revivals were measured for excitation at

345 nm excitation wavelength. Since the 365 nm excitation band lies in the vicinity of the monomer excitation band it was also investigated whether excitation at 365 nm leads to a molecule formation process within the helium droplet.

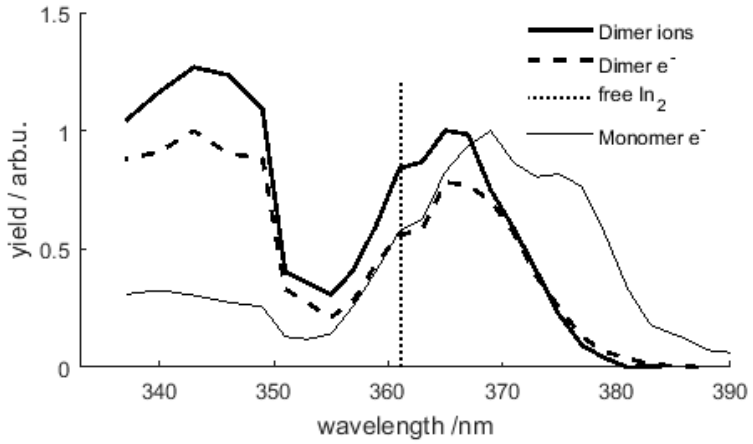

Figure 3.2: Photoexcitation spectrum of indium dimer solvated in He_N: The dotted vertical line marks the excitation wavelength of free In_2 at the $^3\Pi_g(II) \leftarrow {}^3\Pi_u$ transition. The In monomer electron yield is shown for comparison (thin full line). (Lab.Book: 13.07.2017)

3.3 Excitation at the 345 nm Band

At the higher energy excitation band 345 nm, 333 nm and 327 nm were chosen as excitation wavelengths. The WP measurements at 345 nm were conducted for different He_N droplet sizes as well as different frequency doubling crystals in the probe pulse path. Using different frequency doubling crystals has an influence on the spectral and the temporal width of the probe pulse. The experiments were performed with different parameters to optimize the signal. The best results were achieved with the 1 mm thick crystal. The other results are shown here for completeness and to show that the results are reproducible with different experimental parameters. The measured signals were analysed using Sliding Window Fourier Transformation (SWFT), which was however only reasonable when the measurement was continued for more than 10 ps. A detailed description of the SWFT analysis is given in the appendix.

3.3.1 Excitation at 345 nm

The Franck-Condon window for ionisation with 406 nm from the In_2 $^3\Pi_g(II)$ excited state seems to lie at the inner classical turning point of the potential energy curve (see figure 3.3

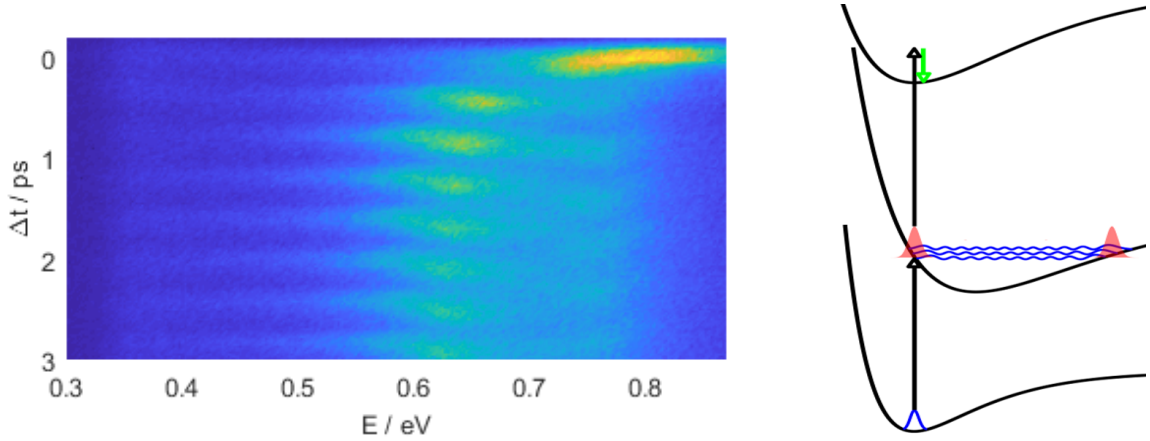

Figure 3.3: Left: Transient PE spectrum at excitation with 345 nm, 406 nm probe wavelength obtained with a 1 mm BBO crystal, 15 K nozzle temperature, 25 fs step size. (Lab.Book: 18.04.2018) Right: Schematic potential energy curves.

on the right). Because the WP is also created at the inner turning point, the measured electron yield exhibits a signal maximum at zero time delay between the pump and the probe pulse, as can be seen in figure 3.3 on the right. The measured PE kinetic energy extends over a wide energy range. The PE peak with the highest amplitude lies at about 0.6 eV. There is another peak with less intensity at about 0.77 eV. This peaks shows a less pronounced energetic shift within the first picosecond than the peak at 0.6 eV. The two PE peaks are in phase within the first picosecond and then move out of phase. Also, when there is a maximum in the electron yield at 0.6 eV, the PE peak extends far to lower kinetic energies.

18 K nozzle temperature, 5 mm LBO crystal

The first coherent vibrational WP dynamics were measured within relatively small He droplets with a mean number of about $\bar{N}$=4800 He atoms (18 K nozzle temperature). These droplets were effectively too small to pick up two atoms that subsequently get excited and probed, many of the droplets were evaporated during pickup and measurement. In the transient PE spectra shown in figure 3.4, the probe laser pulse was frequency doubled to 407 nm with a 5 mm LBO crystal. The probe wavelength was approximately the same in all WP dynamics measurements.

The figures 3.4a,b,c show the primary oscillations of the vibrational WP after its creation, the half revival (HR) around 145 ps pump-probe time delay and the full revival (FR) around 290 ps time delay with their respective Fourier transform (FT) of the spectrum. The results of the SWFT analysis are shown in figure 3.5, again for the primary oscillations, the HR and the FR.

In figure 3.4a the strong energetic shift of the PE peak within the first picosecond after

excitation can clearly be seen. There is also a second smaller PE peak at about 0.78 eV. At 15 ps time delay the two PE peaks are separated by approximately 160 meV. The origin of the signal at 0.78 eV could not be determined so far. The signal vanishes approximately on the same timescale on which the dopant ejection process takes place. In the FT spectrum of the primary oscillations there seems to be a double peak (separated by $\Delta f = 0.07\,THz$). This, however, is most likely due to noise. The higher frequency peak in the double peak structure can not be seen anymore in the FT spectra of the HR and FR. A second peak can also be seen in the FT spectrum of the FR at 1.9 THz (3.4c). This, however, is most likely only a measurement artefact. Intensity fluctuations can be seen in the PE spectrum and this frequency did not appear in other measurements of the FR (see figure 3.8).

In the SWFT spectrum in figure 3.5a the disappearance of the oscillation frequency of 2.4 THz within 10 ps after photoexcitation can be seen. In figures 3.5b and 3.5c a signal at the same frequency can be seen for about 16 ps (FWHM). The increase and decrease of the signal takes about 8 ps. Unfortunately, the resolution of the sliding window spectrogram is not high enough to allow the resolution of the two frequencies in 3.4a. It is not possible to see at what time delay the higher frequency peak disappears.

Attention shall be paid to the fact that the same frequency is observed at the primary oscillations when all, or at least most of the molecules are still immersed in the He_N, and at the FR, when all molecules have left the droplet. This indicates that during the dopant ejection process the WP does not seem to dissipate energy, otherwise an increase in oscillation frequency should be measured. However, it is possible that a frequency increase due to dissipation is compensated by a frequency decrease due to the potential energy curve getting less distorted when the molecule gets ejected from the droplet.

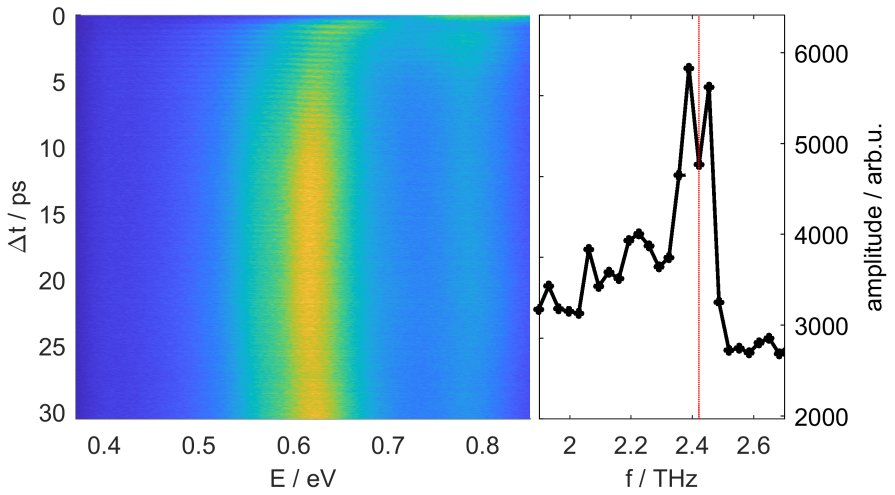

(a) Primary WP oscillations. (Lab.Book: 20.03.2018)

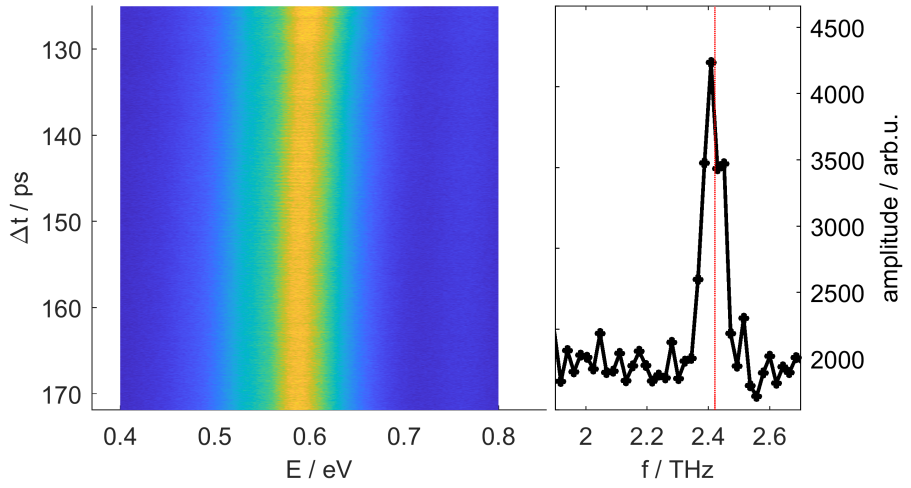

(b) Half revival. (Lab.Book: 21.03.2018)

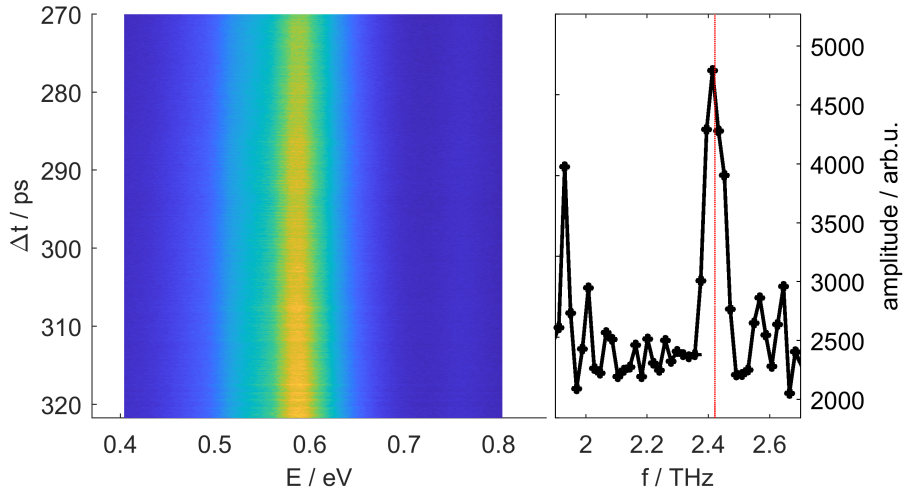

(c) Full revival. (Lab.Book: 22.03.2018)

Figure 3.4: Transient PE spectra (left) and FT (right) of coherent WP oscillations at 345 nm pump wavelength, 407 nm probe wavelength obtained with a 5 mm LBO crystal, 18 K nozzle temperature, 25 fs step size. The red lines in the Fourier spectra indicate the oscillation frequency of 2.42 THz.

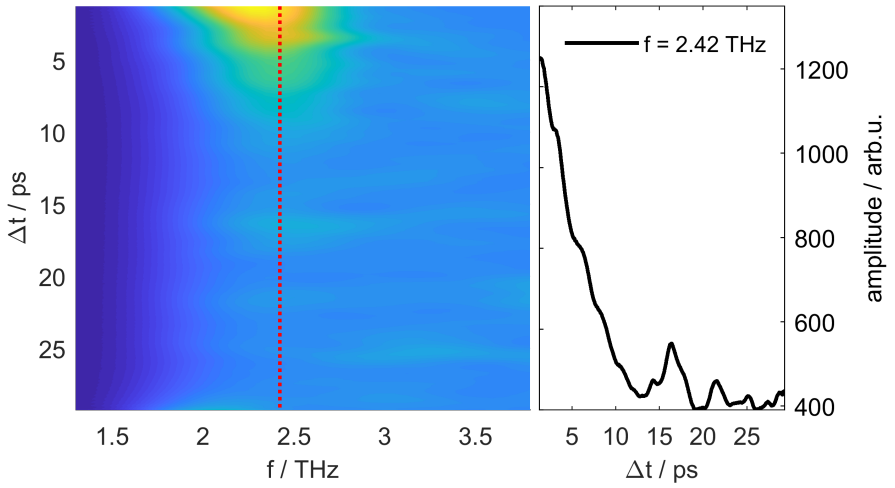

(a) SWFT of primary oscillations.

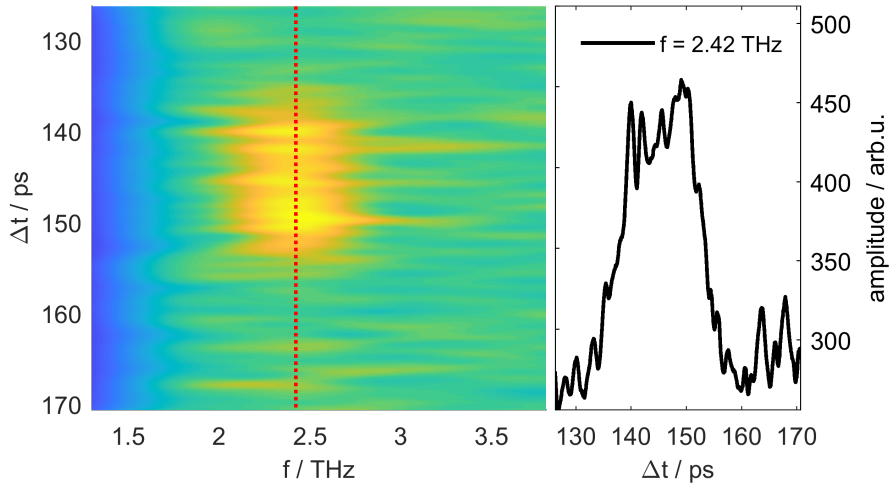

(b) SWFT of half revival.

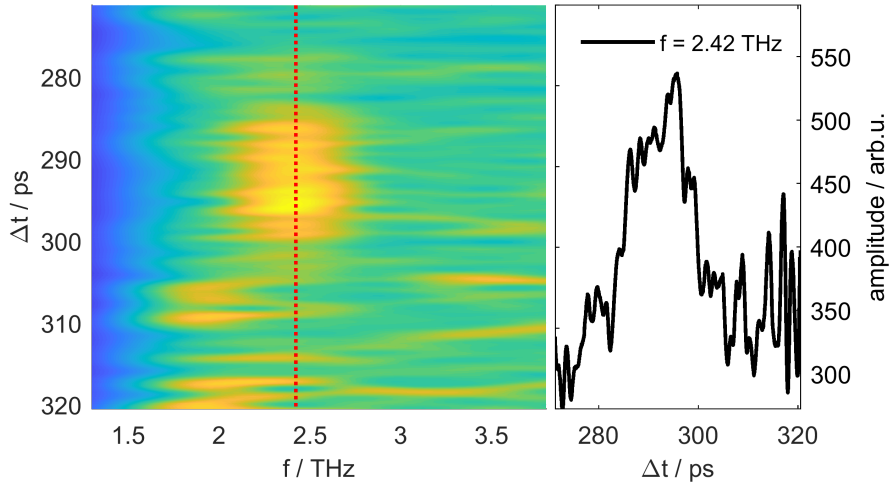

(c) SWFT of full revival.

Figure 3.5: Left: SWFTs of the transient PE spectra shown in figure 3.4a-c, with a window size of 2.5 ps. Right: Cut through the spectrograms at 2.42 THz, indicated on the left by the red vertical line.

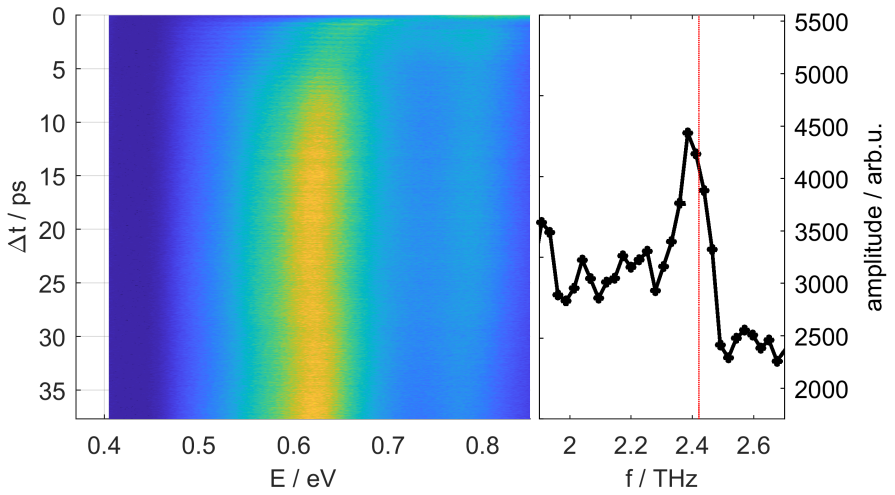

(a) Primary WP oscillations. (Lab.Book: 28.03.2018)

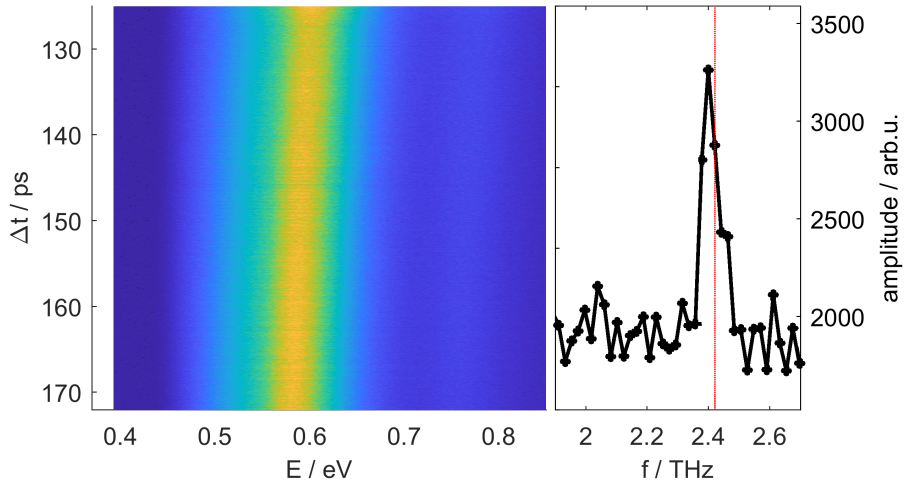

(b) Half revival. (Lab.Book: 29.03.2018)

Figure 3.6: Transient PE spectra (left) and FT (right) of coherent WP oscillations at 345 nm pump wavelength, 406 nm probe wavelength obtained with a 5 mm LBO crystal, 15 K nozzle temperature, 25 fs step size. The red lines in the Fourier spectra indicate the oscillation frequency of 2.42 THz.

15 K nozzle temperature, 5 mm LBO crystal

The next measurement was performed using the same 5 mm LBO crystal. However, the He droplet size was increased to a mean number of $\bar{N}$=8000 He atoms. With these experimental settings on average larger He droplets are doped with In_2 and the measured initial oscillations should mainly stem from dissolved molecules. The transient PE spectra of the primary oscillations and the HR and the corresponding FTs are shown in figure 3.6. No second peak is visible in the Fourier spectrum of the primary oscillations. Again, the

same frequency of 2.4 THz is measured for the primary oscillations and the HR. The SWFT analysis corresponding to this measurement is shown in figure 3.7. As in the previous measurement, the frequency signal of the primary oscillations disappears within about 10 ps. The frequency amplitude corresponding to the HR rises and falls within 8 ps. Unlike before, the oscillation frequency can only be seen for about 13 ps (FWHM), which might be due to a decreased signal-to-noise ratio.

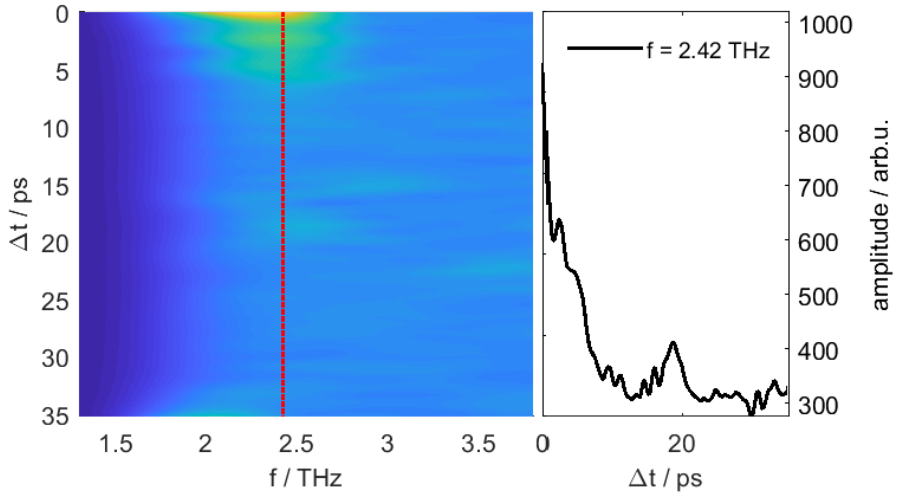

(a) SWFT of primary oscillations.

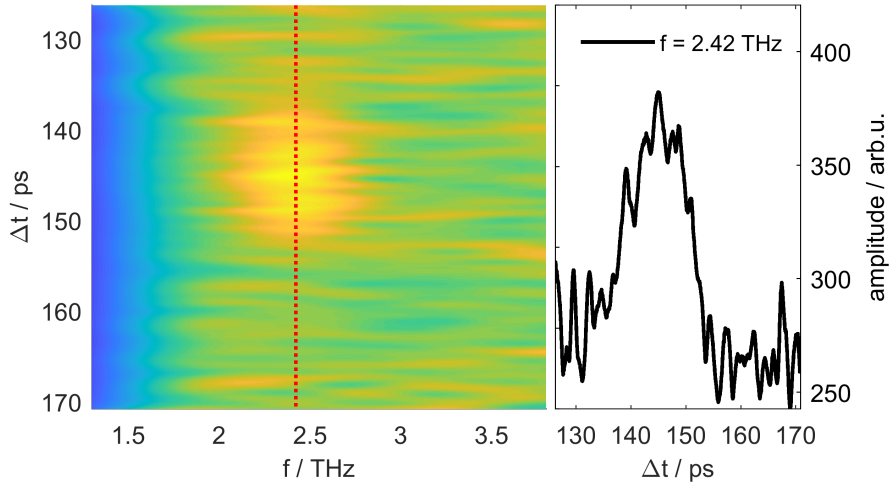

(b) SWFT of half revival.

Figure 3.7: Left: SWFTs of the transient PE spectra shown in figure 3.6a,b, with a window size of 2.5 ps. Right: Cut through the spectrograms at 2.42 THz, indicated on the left by the red vertical line.

15 K nozzle temperature, 1 mm BBO crystal

The measurement of the coherent WP oscillations was repeated doping large He droplets, however, the frequency doubling crystal in the probe laser path was changed for a 1 mm BBO crystal. A shorter crystal within the beam path causes less temporal broadening of the laser pulse, which ensures a better temporal resolution. Albeit, a decreased energy resolution has to be accepted.
The transient PE spectra of the primary oscillations, the HR and the FR are shown in figure 3.8 with their respective FTs. The primary oscillations can clearly be seen in the PE spectrum and the signal-to-noise ratio highly increased with respect to the measurements taken with the thicker LBO frequency doubling crystal. Higher temporal resolution is therefore preferable in the WP dynamics measurement.
Considering the FT of the primary oscillations in figure 3.8a there appears again a double peak structure (peaks separated by $\Delta f = 0.09\,\mathrm{THz}$), again probably caused by noise. As can be seen in the transient PE spectrum, the higher energy peak is not as clearly visible as it has been in the previous measurement at 18 K nozzle temperature (compare figure 3.4a), which might be due to the decreased energy resolution. The peak in the FT of the primary oscillations is clearly broadened compared to the FTs of the HR and the FR (see figure 3.8). It also exhibits a shoulder toward lower oscillation frequencies, which does not seem to be an artefact, and might be due to the energetic shift within the first picosecond after photoexcitation. The peak in the HR Fourier spectrum does not exhibit a shoulder toward lower frequencies anymore. However, considering the red dotted line at 2.42 THz, the peak in the Fourier spectrum at the HR seems broadened toward lower frequencies. The peak in the Fourier spectrum at the FR is more symmetric with respect to the line at 2.42 THz. These observations suggest that immersed In_2 molecules oscillate with slightly lower frequencies than free In_2.
The SWFT analysis for this measurement is shown in figure 3.9. The frequency signal corresponding to the primary oscillations again decreases within 10 ps. The signals of the HR and the FR can be seen for about 17 ps and 14 ps (both FWHM), respectively. The plateaus are less wide and the rise and fall off the signal are longer (about 10 ps) than compared to the signal in figure 3.5.

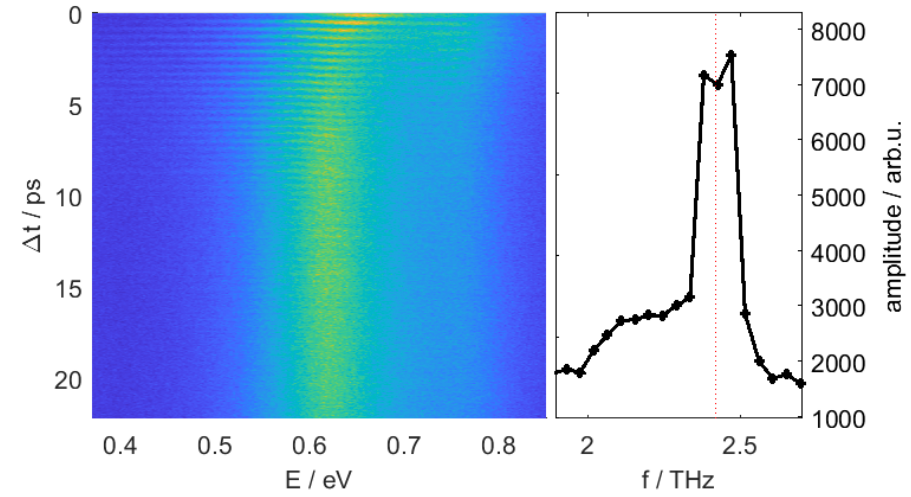

(a) Primary WP oscillations. (Lab.Book: 18.04.2018)

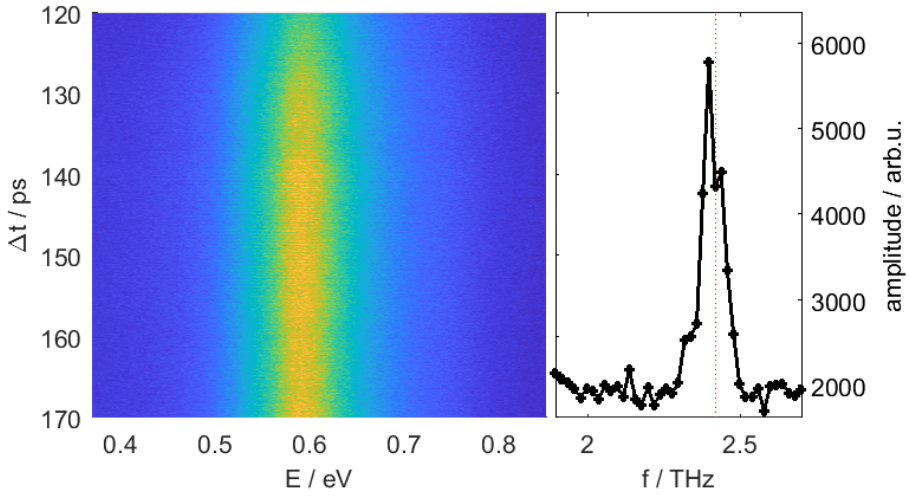

(b) Half revival. (Lab.Book: 18.04.2018)

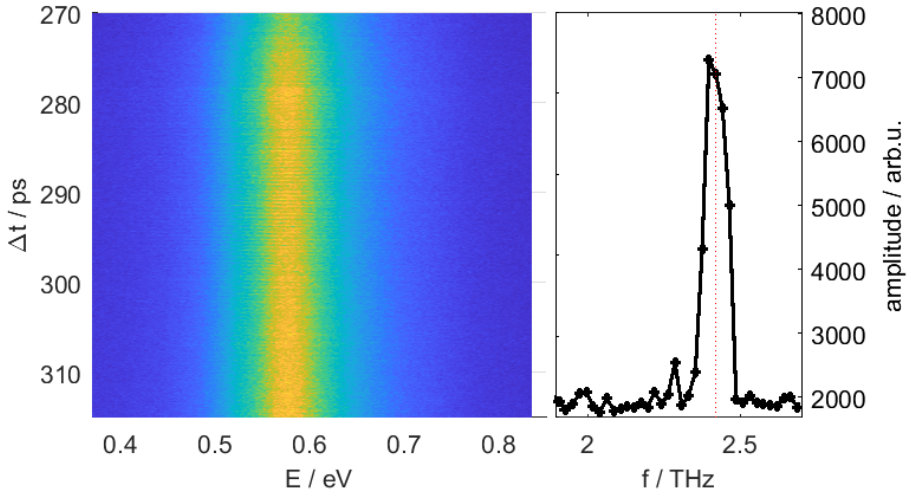

(c) Full revival. (Lab.Book: 19.04.2018)

Figure 3.8: Transient PE spectra (left) and FT (right) of coherent WP oscillations at 345 nm pump wavelength, 406 nm probe wavelength obtained with a 1 mm BBO crystal, 15 K nozzle temperature, 25 fs step size. The red dotted lines in the Fourier spectra indicate the oscillation frequency of 2.42 THz.

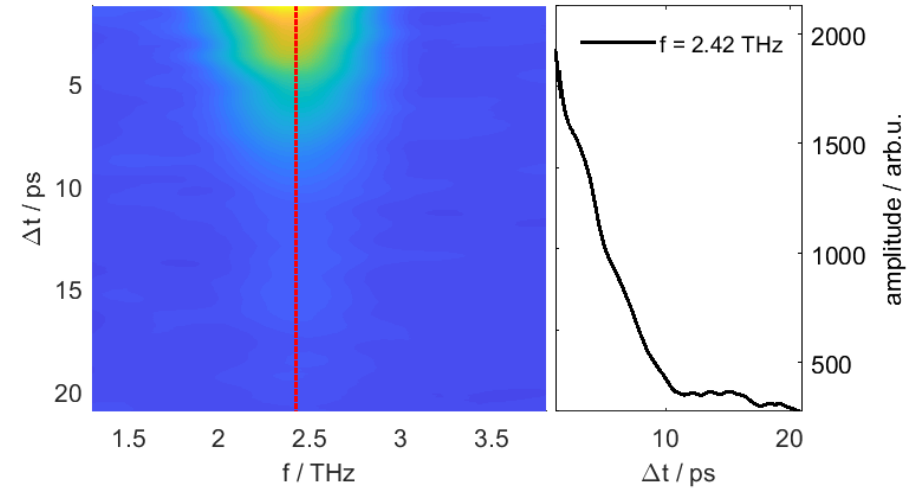

(a) SWFT of primary oscillations.

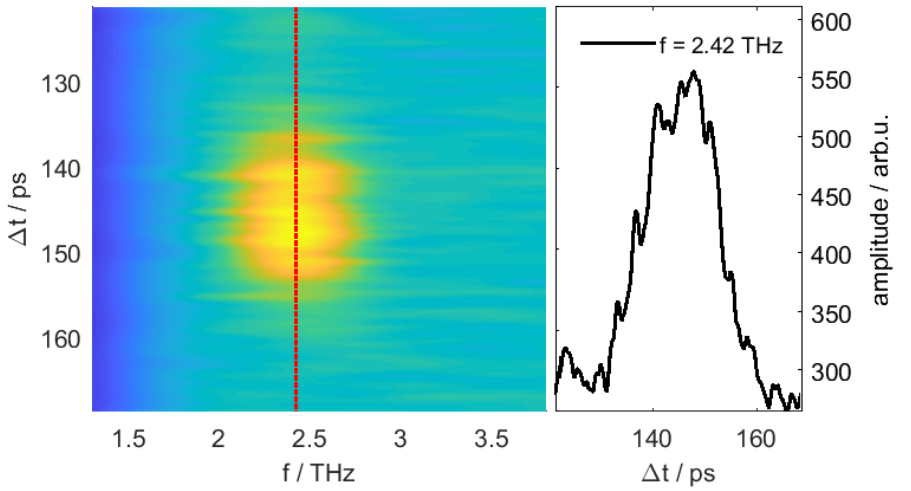

(b) SWFT of half revival.

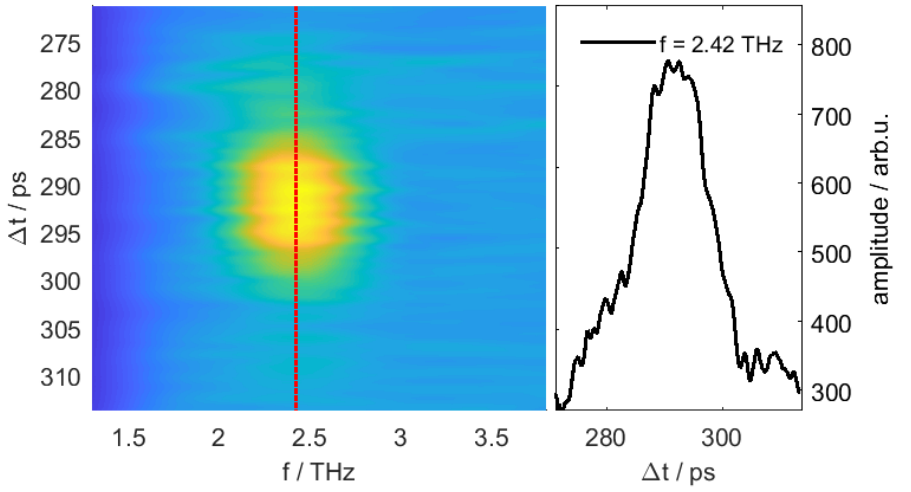

(c) SWFT of full revival.

Figure 3.9: Left: SWFTs of the transient PE spectra shown in figure 3.8a-c, with a window size of 2.5 ps. Right: Cut through the spectrograms at 2.42 THz, indicated on the left by the red vertical line.

3.3.2 Compare results for 1 mm BBO to 5 mm LBO crystal

As mentioned before, two different frequency doubling crystals were used in the measurement of the coherent WP dynamics at 345 nm excitation wavelength. Figure 3.10 shows the integrated electron yield within the first four picoseconds after photoexcitation for measurements in which the different crystals were used. Probing the WP using the BBO crystal gave a much better signal-to-noise ratio, even though the data acquisition time was reduced by about 30% with respect to the measurement using the LBO crystal ($3*10^4$ laser shots compared to $5*10^4$ laser shots). The signal contrast increased from about 10% using the thicker LBO to about 20% using thinner BBO crystal. A good temporal resolution obviously has a striking influence on the oscillation contrast. This seems reasonable if one considers that ionisation of the localised WP occurs within the Franck-Condon window. The WP travels one round-trip within about 400 fs. The probe pulse needs to be considerably shorter than this in order for the electron yield to show a large contrast.

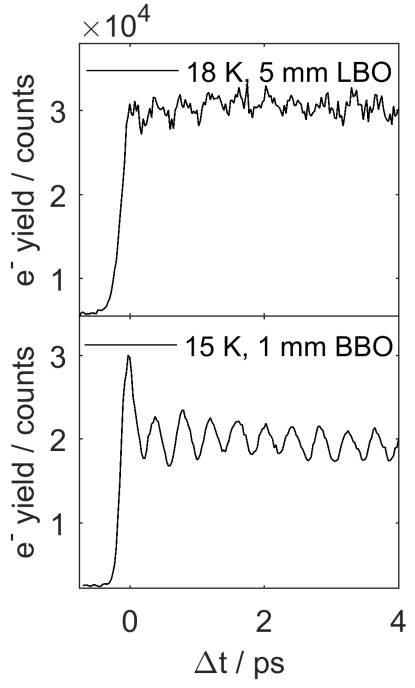

Figure 3.10: Total electron yield measured with a 5 mm LBO crystal (top) compared to a 1 mm BBO crystal (bottom) in the probe beam path for frequency doubling.

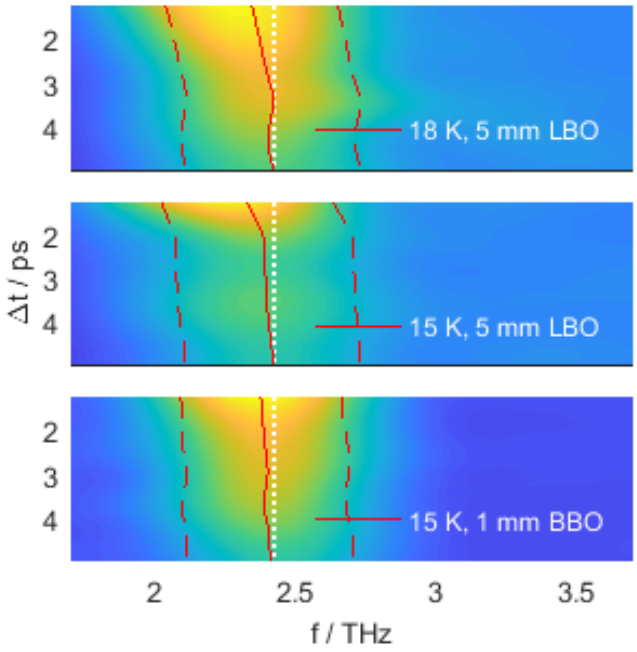

Figure 3.11: Frequency shift of WP oscillations after photoexcitation at 345 nm excitation wavelength. Full red lines: Barycentre calculated from the SWFT signals between 1.8 THz and 2.8 THz. Dashed red lines: Confidence intervals. Dashed white lines: Oscillation frequency of 2.42 THz.

Comparing the first five picoseconds of the SWFT analysis of the primary oscillations measured with three different experimental parameters, it can be seen that a small frequency shift from lower to higher frequencies occurs right after photoexcitation (see figure 3.11). While the shift is clearly visible for the measurements done with the thicker LBO crystal, the shift is hardly visible when frequency doubling was done with the thinner BBO crystal. This could be due to the higher energy resolution obtained with the thicker crystal. It has to be considered, however, that the window in the SWFT analysis has a size of 2.5 ps. A possible bias of the frequency shift due to pump-probe cross correlation effects has to be kept in mind. Also the influence of a possibly chirped excitation pulse on the shift and decay of the primary oscillation frequency is not yet fully understood.

In conclusion, a good temporal resolution is desirable for a large contrast in the oscillation signal and if one wants to reduce data acquisition time. However, to resolve a small frequency shift, a higher energy resolution is more advantageous, because FT is a powerful tool to distinguish even small periodic modulations from noise.

3.3.3 Excitation at 333 nm

The coherent WP dynamics excited at 333 nm pump wavelength can be seen in the transient PE spectrum shown in figure 3.12 with its respective FT. Two transient PE peaks can clearly be seen. The higher energy peak is more pronounced than at excitation with 345 nm (compare figure 3.8a). Also, it initially exhibits a larger amplitude, which decreases within about 10 ps after photoexcitation, while the amplitude of the lower energy peak increases within the same time frame (see figure 3.13). Comparing the transient PE spectrum with the one obtained for excitation at 345 nm, the higher energy PE peak exhibits now also the shift to lower energies within 1 ps that is characteristic for the bubble expansion. At 15 ps time delay the two PE peaks are separated by about 140 meV. The signal-to-noise ratio of the Fourier spectrum is quite low and the actual oscillation frequency of the WP can not be determined unequivocally from this spectrum. Therefore, FTs were performed separately for the two different PE peaks, starting at 0.5 ps time delay. The result is shown in figure 3.14. The lower PE energy peak, between 0.50 eV and 0.70 eV, oscillates at 2.4 THz, the higher one, between 0.70 eV and 1.05 eV, oscillates at 2.1 THz.

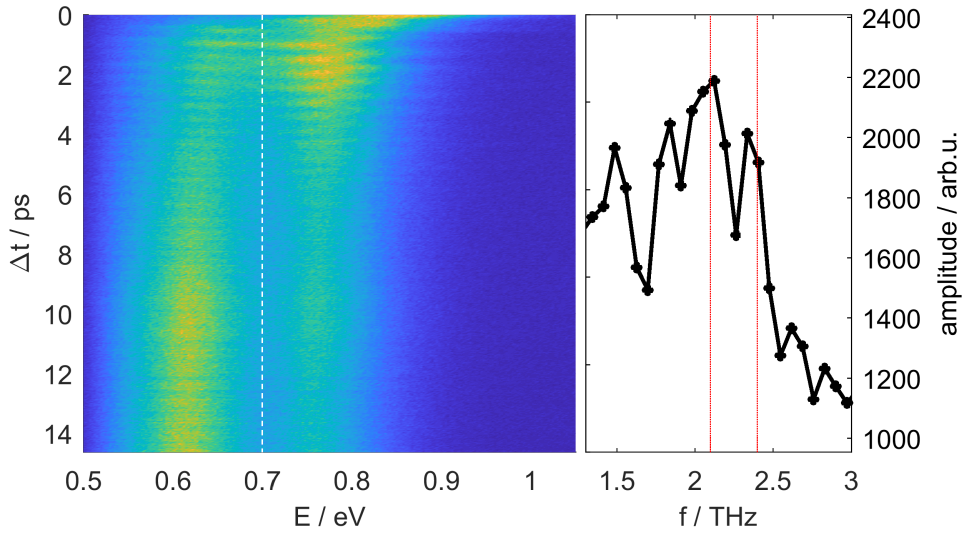

Figure 3.12: Primary WP ocsillations. Transient PE spectrum (left) and FT (right) of coherent WP oscillations at 333 nm pump wavelength, 405 nm probe wavelength obtained with a 5 mm LBO crystal, 15 K nozzle temperature, 25 fs step size. The FT was performed from 0.5 ps time delay onward. The red lines in the Fourier spectrum indicate the oscillation frequencies of 2.1 THz and 2.4 THz, respectively. The white dashed line in the PE spectrum indicates the threshold between the higher and lower PE energy peak. (Lab.Book: 05.04.2018)

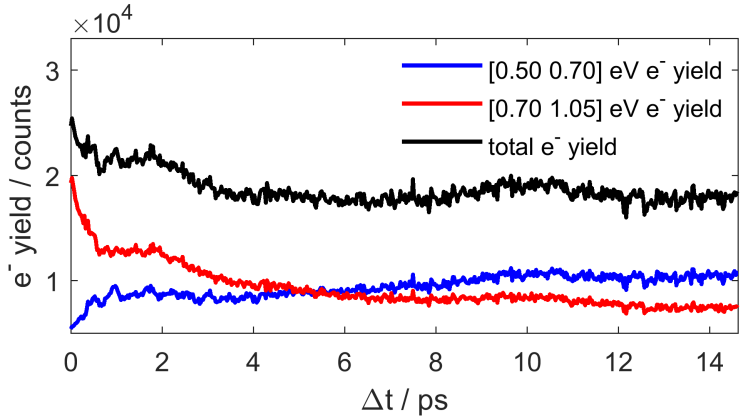

Figure 3.13: Blue line: Integrated electron yield of the lower PE energy peak (between 0.50 eV and 0.70 eV). Red line: Integrated electron yield of the higher PE energy peak (between 0.70 eV and 1.05 eV) shown in figure 3.12. Black line: Total electron yield. The strong in-, respectively decrease, within the first picosecond corresponds to the shift to lower kinetic energies due to the bubble expansion and the pump-probe cross correlation signal.

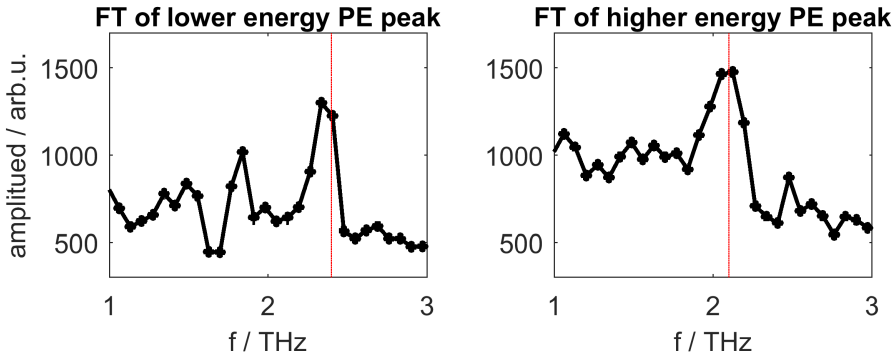

Figure 3.14: Separate FT of higher and lower PE energy peak, starting from 0.5 ps time delay. Left: The lower energy peak oscillates at 2.4 THz (red line). Right: the higher energy peak oscillates at 2.1 THz (red line). Two peaks at the same oscillation frequencies can be seen in the Fourier spectrum shown in figure 3.12 on the right.

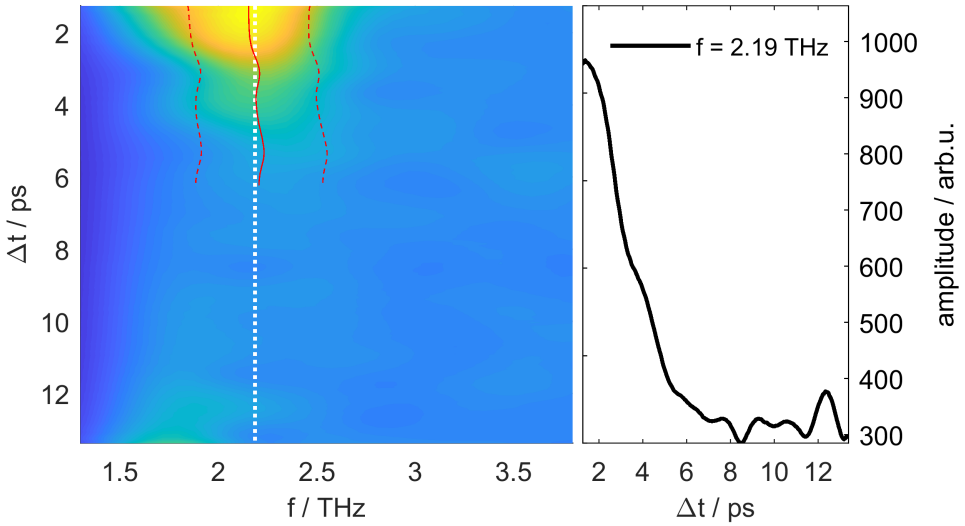

Figure 3.15: Left: SWFT of the transient PE spectrum shown in figure 3.12, with a window size of 2.5 ps. The full red line indicates the barycentre calculated from the SWFT signal between 1.64 THz and 2.74 THz, the dashed red lines indicate the confidence interval. Right: Cut through the spectrogram at 2.19 THz, indicated on the left by the white dotted line.

The SWFT analysis of these WP dynamics is shown in figure 3.15. The amplitude of the oscillation frequency of 2.19 THz decreases within about 6 ps, which is considerably faster than at excitation with 345 nm (see figure 3.9). A lower oscillation frequency for excitation with a higher photon energy is the result that is expected in a Morse like potential. The barycentre of the oscillation frequency (full red line in figure 3.15 on the left) seems to move slightly toward higher vibrational frequencies with increasing pump-probe time delay. However, the same considerations as for excitation at 345 nm, namely a possibly

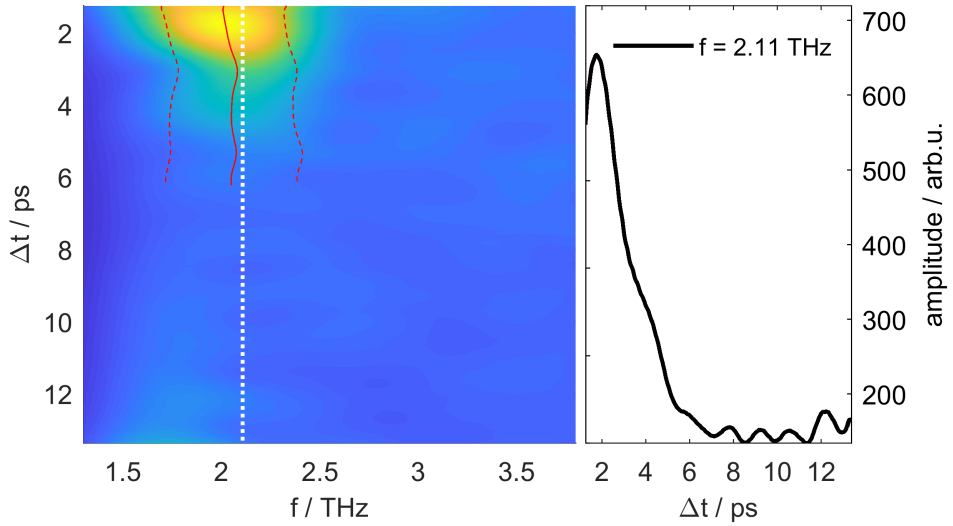

Figure 3.16: Left: SWFT of the transient PE spectrum shown in figure 3.12 between 0.70 eV and 1.05 eV, with a window size of 2.5 ps. The full red line indicates the barycentre calculated from the SWFT signal between 1.6 THz and 2.9 THz, the dashed red lines indicate the confidence interval. Right: Cut through the spectrogram at 2.11 THz, indicated on the left by the white dotted line.

chirped excitation pulse and pump-probe cross correlation effects, have to be taken into account.

Separate SWFTs have been performed for the higher and lower PE energy peak shown in figure 3.12. The result for the higher energy peak can be seen in figure 3.16, where the SWFT was performed between 0.70 eV and 1.05 eV. It can be seen that the oscillation amplitude at 2.1 THz decreases within 6 ps. The oscillation frequency shifts slightly to higher values within about 3 ps.
The SWFT analysis of the lower energy PE peak can be seen in figure 3.17, which was performed between PE energies of 0.50 eV and 0.70 eV. The oscillation frequency does not seem to shift to higher values and the amplitude at about 2.4 THz decreases within 8 ps and therefore slower than the oscillation frequency of the higher energy PE peak.

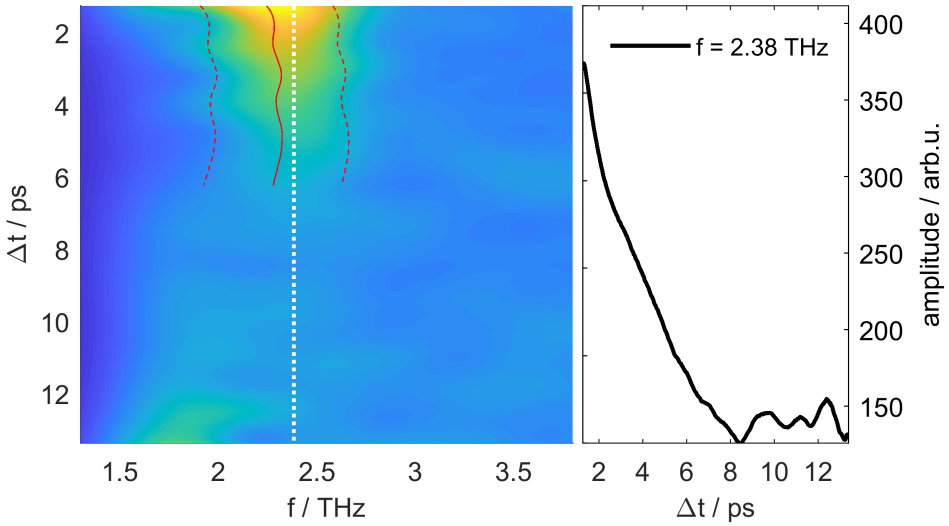

Figure 3.17: Left: SWFT of the transient PE spectrum shown in figure 3.12 between 0.50 eV and 0.70 eV, with a window size of 2.5 ps. The full red line indicates the barycentre calculated from the SWFT signal between 1.4 THz and 2.6 THz, the dashed red lines indicate the confidence interval. Right: Cut through the spectrogram at 2.38 THz, indicated on the left by the white dotted line.

3.3.4 Excitation at 327 nm

Figure 3.18 shows the transient PE spectrum obtained with excitation at 327 nm pump wavelength. The spectrum was only recorded until 5 ps time delay, which made an analysis with SWFT not feasible. The FT does exhibit a peak in the frequency range, where oscillations are expected, however, for a trustworthy analysis the measurement has to be repeated up to longer pump-probe time delays.

In the measured spectrum in figure 3.18 the two PE peaks at different energies can still be distinguished, however not as clearly. This might be a consequence of the lower energy resolution of the probe laser beam, when it is frequency doubled with the 1 mm BBO crystal. The higher energy peak exhibits again the energetic shift due to the bubble expansion, even more clearly so than at excitation with 333 nm. It shall be noted here that the energetic separation between the two PE peaks is approximately 150 meV for all of the three different wavelengths 345 nm, 333 nm and 327 nm.

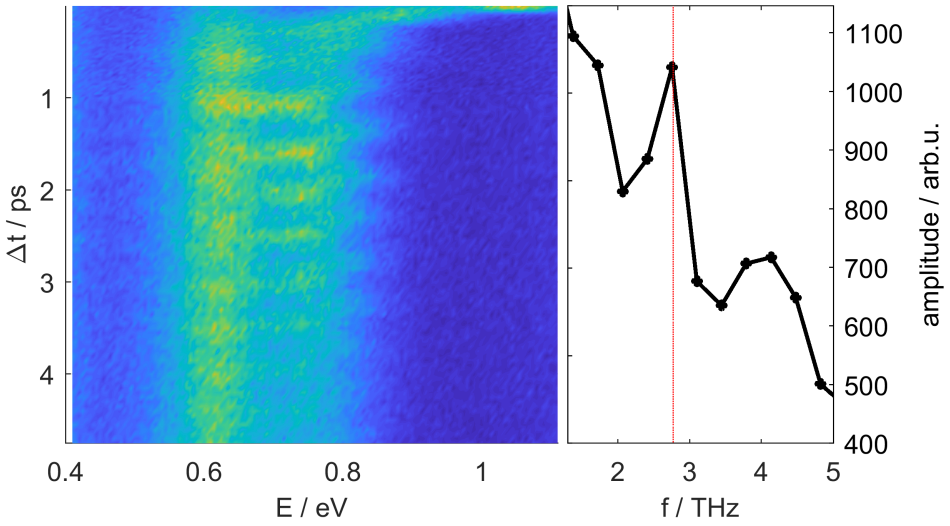

Figure 3.18: Primary WP ocsillations. Transient PE spectrum (left) and FT (right) of coherent WP oscillations at 327 nm pump wavelength, 405 nm probe wavelength obtained with a 1 mm BBO crystal, 18 K nozzle temperature, 25 fs step size up to 1 ps time delay, then 50 fs step size. The red dotted line in the Fourier spectrum indicates the oscillation frequency of 2.76 THz. (Lab.Book: 24.11.2017)

3.4 Excitation at the 365 nm Band

3.4.1 Excitation at 360 nm

The second identified energy band of In_2 within superfluid He_N is centred around 365 nm (see figure 3.2). The transient PE spectrum obtained with excitation at 360 nm is shown in figure 3.19. The time steps in the measurement were chosen too coarsely for the FT to give a reasonable result. In the spectrum two PE peaks at two different energies can be seen, with a large amplitude in the higher and a small amplitude in the lower energy peak. The peak at about 0.30 eV stems from In monomer.

Integrating the PE signal between 0.20 eV and 0.45 eV and between 0.45 eV and 1.0 eV results in the two curves shown in figure 3.20. Minima in the yield of higher energetic PEs coincide with maxima in the yield of lower energetic PEs. The signal modulation after 3 ps time delay is too small to distinguish any more maxima or minima.

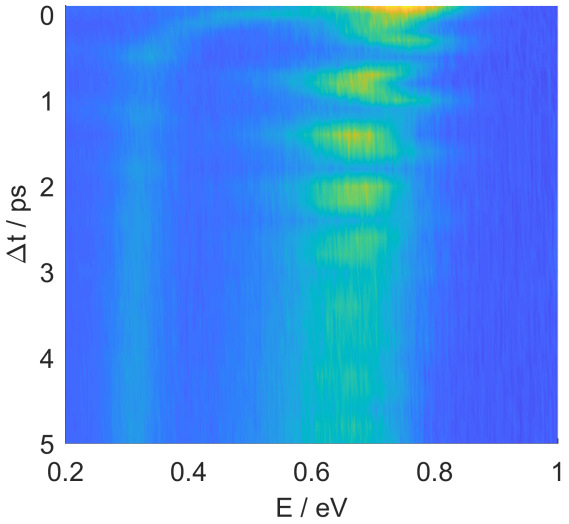

Figure 3.19: Primary WP oscillations. Transient PE spectrum of coherent WP oscillations at 360 nm pump wavelength, 405 nm probe wavelength obtained with a 1 mm BBO crystal, 18 K nozzle temperature, 100 fs step size up to 1.2 ps time delay, then 200 fs step size. (Lab.Book: 21.11.2017)

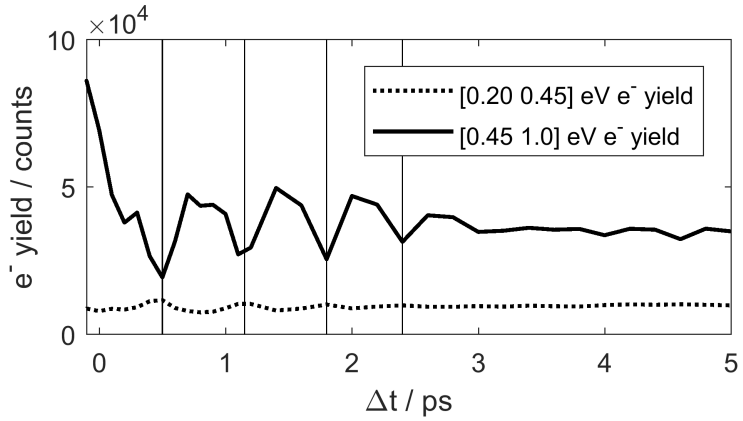

Figure 3.20: Dotted line: Integrated electron yield of the lower PE energy peak (between 0.20 eV and 0.45 eV). Full thick line: Integrated electron yield of the higher PE energy peak (between 0.45 eV and 1.0 eV) shown in figure 3.19. The strong decrease of the higher energetic electron yield within the first picosecond corresponds to the pump-probe cross correlation signal. The vertical lines indicate minima, respectively maxima, in the higher, respectively lower energy PE yield.

3.4.2 Excitation at 365 nm

The transient PE spectrum obtained for excitation at 365 nm is shown in figure 3.21 with the corresponding FT. At this excitation wavelength only one PE peak is visible in the energy spectrum. Electrons that stem from In monomer do not reach the detector, because a larger positive voltage had been applied to the repeller for better energy resolution of the In_2 peak. The spectrum was calibrated energetically according to a PE spectrum at high pump probe time delay obtained with excitation at 370 nm, where the In monomer and dimer peak were clearly visible. A designated calibration measurement for excitation at 365 nm shall be done in the future.

In the frequency spectrum there is a large peak at 1.5 THz, however, the oscillation frequency of 1.80 THz (indicated by the red dotted line in the Fourier spectrum) persists for more than 3 ps. The corresponding SWFT analysis can be seen in figure 3.22. There is a very strong decrease of oscillation amplitude within only 3 ps. The oscillations at 1.80 THz seem to continue for more than 10 ps, unfortunately the measurement was aborted before the WP had completely dispersed.

The frequency shift indicated by the full red line in figure 3.22 can be resolved even though the pump laser pulse was frequency doubled with the 1 mm BBO crystal. Figure 3.23 shows the FT of the transient PE spectrum at 365 nm excitation wavelength (figure 3.21) up to 4 ps (left) and from 4 ps up to 12 ps time delay (right). At short time delay an oscillation frequency of 1.5 THz is found. While at larger pump-probe time delay the molecule oscillates at 1.8 THz. This increase of oscillation frequency within about 4 ps could stem from energy dissipation. The attempt to find a revival at this excitation wavelength was not successful.

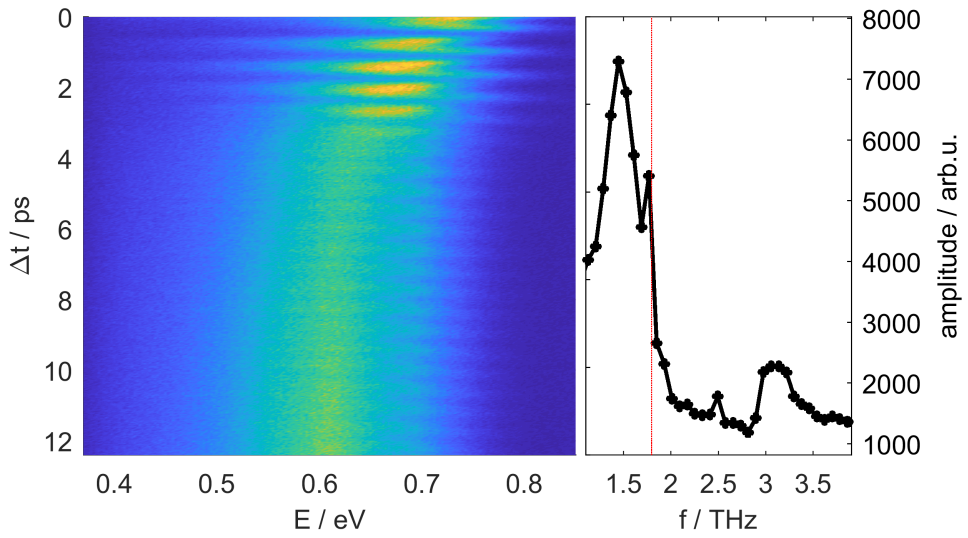

Figure 3.21: Primary WP ocsillations. Transient PE spectrum (left) and FT (right) of coherent WP oscillations at 365 nm pump wavelength, 404 nm probe wavelength obtained with a 1 mm BBO crystal, 15 K nozzle temperature, 25 fs step size. The red line in the Fourier spectrum indicates the oscillation frequency of 1.80 THz. (Lab.Book: 03.05.2018)

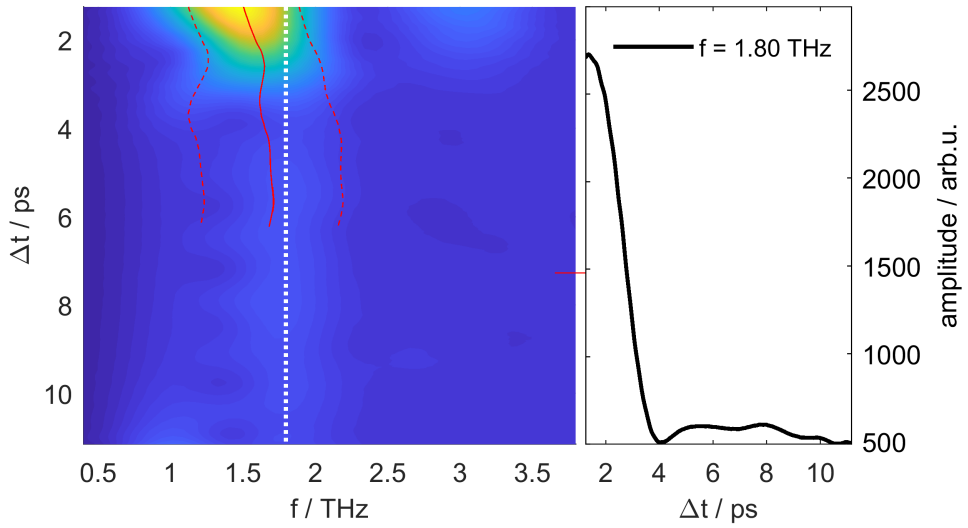

Figure 3.22: Left: SWFT of the transient PE spectrum shown in figure 3.21, with a window size of 2.5 ps. The full red line indicates the barycentre calculated from the SWFT signal between 0.7 THz and 2.6 THz, the dashed red lines indicate the confidence interval. Right: Cut through the spectrogram at 1.80 THz, indicated on the left by the white dotted line.

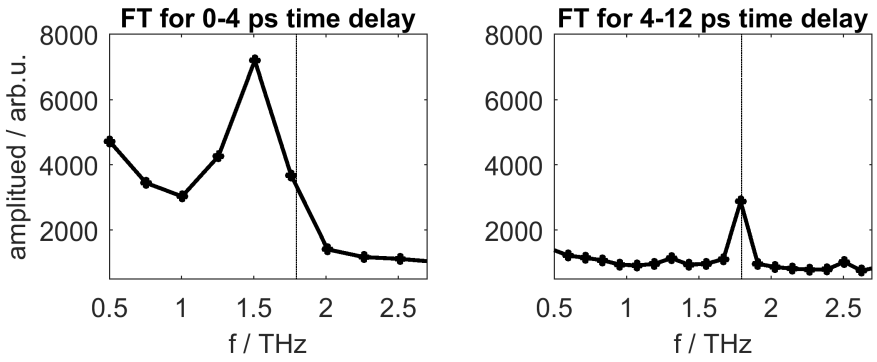

Figure 3.23: FT of the PE spectrum shown in figure 3.21 between 0 ps and 4 ps pump probe time delay (left) and between 4 ps and 12 ps (right). The vertical lines indicate 1.80 THz. Within the first 4 ps after photoexcitation the oscillation frequency increases from 1.50 THz to 1.80 THz. This could be due to dissipation.

3.4.3 Compare WP oscillations for excitation at 345 nm and 364 nm

Two excitation bands have been identified for In_2, as can be seen in figure 3.2. The coherent WP dynamics excited at the two center wavelengths, namely 345 nm and 365 nm, show different behaviours. For excitation at 345 nm the oscillation frequency of the WP was found to be 2.4 THz and a half revival as well as a full revival of the WP were measured. Excitation at 365 nm initiated WP oscillations at 1.8 THz and no revivals could be measured so far. In figure 3.24 the first few picoseconds of the transient PE spectra obtained for excitation at 345 nm (right) and 365 nm (left) are shown. For excitation at 365 nm the PE peak does not exhibit the strong shift to lower energies within the first picosecond after photoexcitation that is characteristic for the bubble expansion process. The maxima in the PE spectrum are U-shaped. For excitation at 345 nm the bubble expansion peak shift can clearly be seen and the maxima have an elongated shape. At the same time delay, at which a signal minimum is measured after 345 nm excitation, a signal maximum is obtained after 365 nm excitation. A possible reason for this is that the WP is excited with 365 nm at the outer turning point of the potential curve of In_2. Another explanation is that the WP is created at the inner, but probed at the turning point.

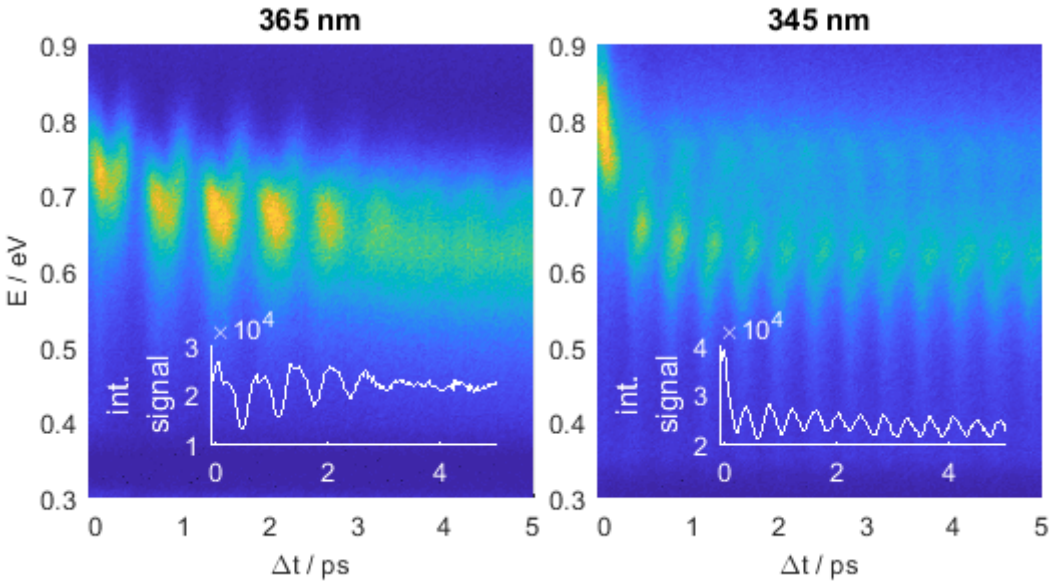

Figure 3.24: Comparison of the transient PE spectra obtained for excitation with 365 nm (left, see also figure 3.21) and 345 nm (right, see also figure 3.8a). The insets show the integrated electron yields.

Table 3.1 lists the energies of the pump and probe pulses that were used in the measurements to obtain the transient PE spectra shown in figure 3.24. After 5 ps the PE peak

has reached approximately 0.61 eV for both excitation wavelengths. This suggests that the same electronic state is excited with the two different wavelengths. The difference in the summed up photon energies of 6.64 eV and 6.47 eV matches approximately the energy that gets converted during the bubble expansion process at excitation with 345 nm.

Table 3.1: Pump and probe pulse energies

	Wavelength / nm	**Energy / eV**	**Wavelength / nm**	**Energy / eV**
Pump	345	3.59	365	3.40
Probe	406	3.05	404	3.07
Sum		6.64		6.47

3.5 Investigate Possible Foam Collapse

It has been found that when one He_N is doped with several Mg atoms, each one resides in its own solvation shell, separated from the others by a He barrier [39, 40]. The agglomerate of different solvation shells is called "foam". Upon photoexcitation of one single Mg atom the foam collapses and a Mg cluster forms. Since the excitation band of In_2 in He_N around 365 nm excitation wavelength overlaps with the In momonomer in He_N excitation band (see figure 3.2 and reference [50]), the idea arose that the In_2 yield at this excitation band stems from dimers formed after a foam collapse as it has been observed for Mg. If this was the case, also a considerable yield of In trimer would be suspected.
Another explanation for the excitation band around 365 nm could be that a different ground state (the $^3\Sigma_g$, see figure 1.4) is populated as well. This would allow for excitation of a different electronic excited state than the $^3\Pi_g$(II).
The ion yield in figure 3.25 was obtained at a high pump-probe time delay and for a nozzle temperature of 18 K, which corresponds to a mean number of $\bar{N} = 4800$ He atoms. High peaks representing the In and In_2 yield at 115 amu respectively 230 amu were detected, however, no significant amount of In_3 was measured (23 counts within the mass interval from 325 amu to 360 amu). The He droplets in this measurement had been relatively small and therefore not been optimized for trimer pickup. The lack of trimer signal could have been caused by evaporated He droplets and In_3 breaking apart again before reaching the detector. Therefore the experiment was repeated for nozzle temperatures of 15 K and 13 K, which corresponds to a mean number of approximately $\bar{N} = 8000$, respectively $\bar{N} = 13000$ He atoms. The ion yield was measured at 2 ps and 300 ps pump-probe time delay, also the current heating the pick up cell was increased for a higher In vapour pressure. The results are shown in figure 3.26. Still no significant amount of In trimer was measured (about 100 counts within the 325 amu to 360 amu mass interval). There is no increase of

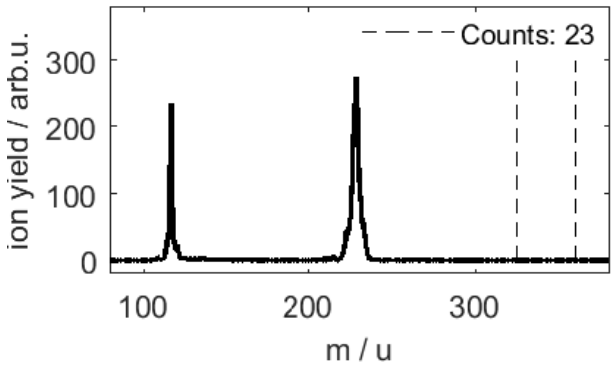

Figure 3.25: Ion yield at large pump probe time delay obtained at 365 nm excitation wavelength, 18 K nozzle temperature and 43 A pick up current. There are two large peaks, one at the In mass (115 u) and one at the In_2 mass (230 u). Within the mass interval from 325 u to 360 u (indicated by the dashed vertical lines) 23 counts were detected. (Lab.Book: 27.11.2017)

the In_3 yield from short to long time delays. At short pump-probe time delay a larger yield of In-He_n complexes than In or In_2 is detected, because most In atoms and molecules are still immersed in the droplet. For a discussion on complex formation see section 3.6 below.

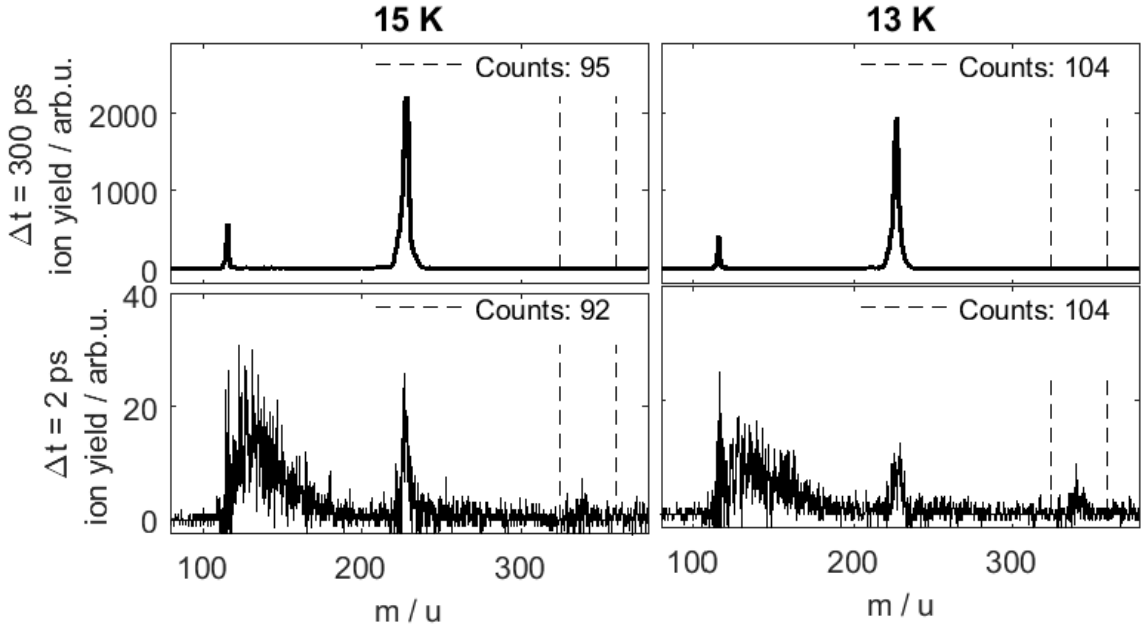

Figure 3.26: Ion yield at 2 ps (bottom) and 300 ps (top) pump probe time delay obtained at 365 nm excitation wavelength, 15 K (left), respectively 13 K (right) nozzle temperature and 44 A pick up current. There is a significant yield of In-He_n complexes as short pump-probe time delay, however still very few In_3 counts. (Lab.Book: 27.04.2018)

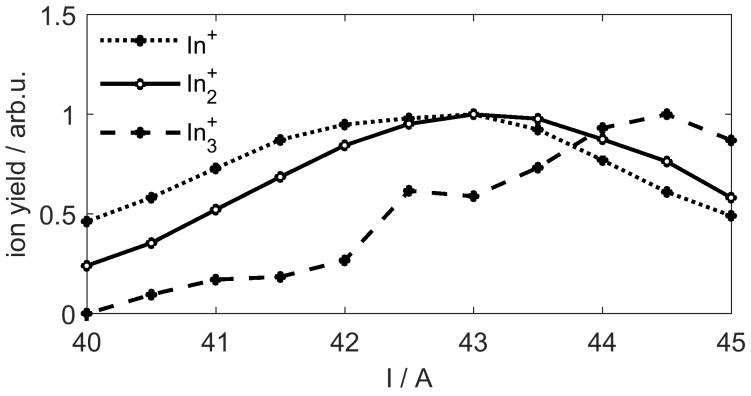

Figure 3.27: Ion yield obtained at large pump probe time delay at 365 nm excitation wavelength, 404 nm probe wavelength and 13 K nozzle temperature as a function of pick up current. Full line: In_2 yield. Dotted line: In yield. Dashed line: In_3 yield. The curves are amplitude normalised. The ratio of the unnormalised maximum monomer:dimer:trimer yield is $0.151 : 1 : 0.002$, the maximum dimer yield is 500 times higher than the maximum trimer yield at excitation with 365 nm. (Lab.Book: 04.05.2018)

Another test to investigate a possible foam collapse was performed in such a way that the nozzle temperature was set to 13 K and the pick up current was systematically varied from 40 A to 45 A. The In monomer, dimer and trimer yields are plotted as a function of pick up current. The resulting graph can be seen in figure 3.27. The dimer yield initially rises with increasing pick up current, peaks and finally drops again. When the dimer yield starts to decrease with increasing pick up current, the trimer yield rises, because of higher trimer pick up probability. However, the maximum In trimer yield at 365 nm excitation wavelength is 500 times lower than the maximum dimer yield. This means that there is In_3 pick up, but its excitation band does not lie around 365 nm. Destroying the He droplets should not be an issue, since the measurement was done with very large droplets. The results of all these investigations make an In foam collapse within the He_N very unlikely.

3.6 Exciplex Formation

Measuring the ion charge-to-mass ratio, it was found that at short pump-probe time delays a significant amount of In-He_n complexes are detected. Figure 3.28 on the left shows a transient mass spectrum up to 305 ps after photoexcitation at 345 nm. On the right, the ion yield integrated over the In, In-He_n and In_2 mass intervals is shown as a function

of pump-probe time delay. It can be seen that, initially, mainly exciplexes are detected, while the In and In_2 yields show a delayed onset and rise with increasing time delay, corresponding to the dopant ejection process described in reference [10] and section 3.1. Exciplexes are detected across the entire time delay range with a broad maximum around 40 ps time delay.

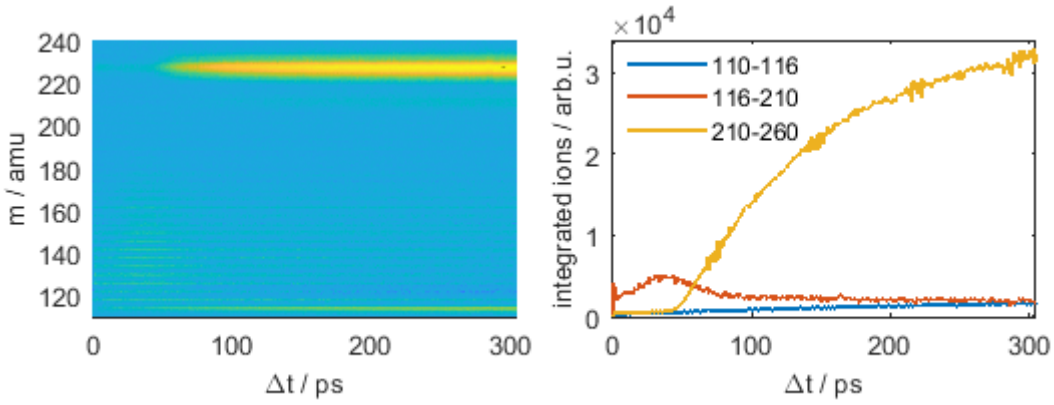

Figure 3.28: Left: Transient mass spectrum up to 305 ps pump-probe time delay at 345 nm pump wavelength and 15 K nozzle temperature. Note that the amplitude of the ion yield is plotted on a logarithmic scale to make the exciplexes with low intensity better visible. Right: Integrated ion yield of In (110 amu to 116 amu, blue line), In-He_n (116 amu to 210 amu, red line) and In_2 (210 amu to 260 amu, yellow line). (Lab.Book: 25.04.2018)

Figure 3.29 shows two exemplary mass spectra from the transient mass spectrum shown in figure 3.28, one at 2 ps and one at 300 ps pump-probe time delay. Again, it can be seen that initially more exciplexes are detected, while at large pump-probe time delay mainly In dimers are detected. The exciplex yield first increases with an increasing number of He atoms attached to the In. When more than $n = 4$ He atoms are attached, the exciplex yield decreases with increasing n.

In order to find out whether the In and the In-He_n yield stems from subsequent ionisation, the ion yield was measured as a function of the pump and probe laser power. The number of ion counts is proportional to the laser power P to the power of m, where m represents the number of photons involved in the process:

$$\text{counts} \propto P^m \tag{3.1}$$

This means that in a log-log plot of the ion yield versus laser power, the slope of the curve should be, for example, $m = 1$ if one photon is involved in the ionisation. In figure 3.30

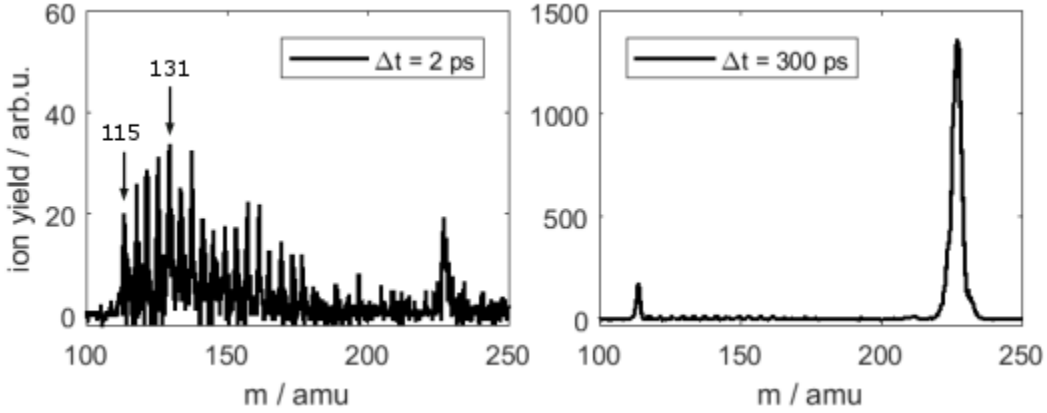

Figure 3.29: Mass spectra at 2 ps (left) and 300 ps (right) time delay, at 345 nm pump wavelength and 15 K nozzle temperature. (Lab.Book: 25.04.2018)

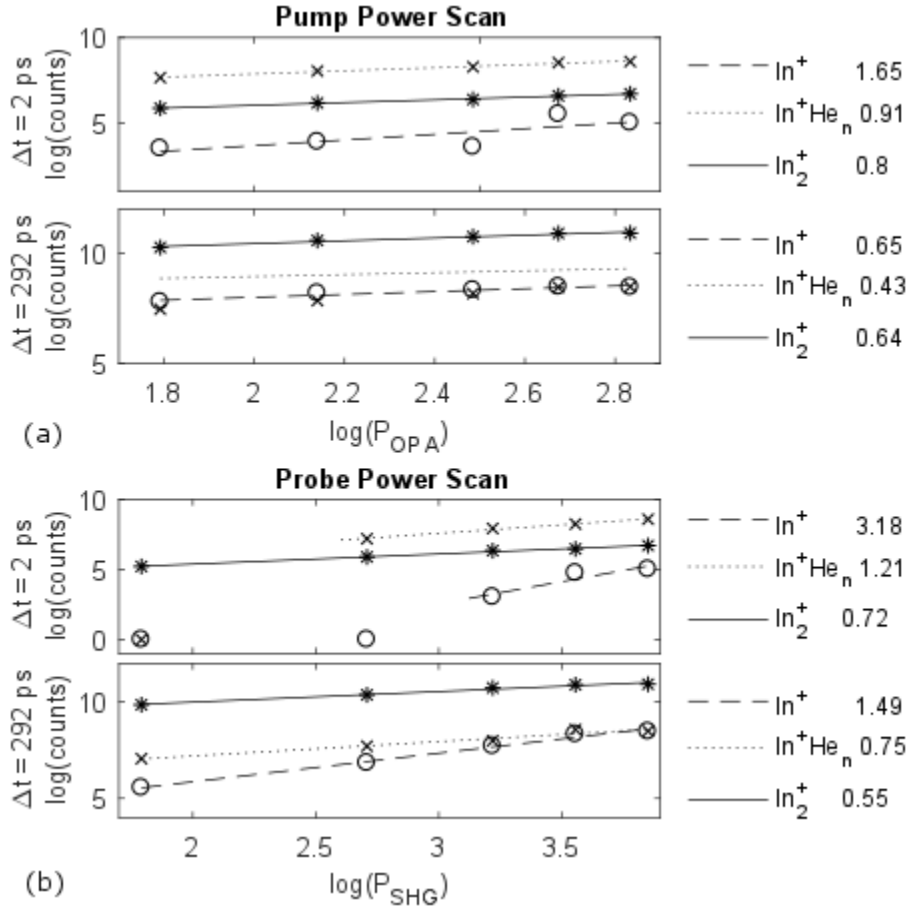

Figure 3.30: Variation of laser pulse power to identify how many photons are involved in the excitation an ionisation process: (a) Variation of pump pulse power and (b) variation of probe pulse power at 2 ps and 292 ps pump-probe time delay. The slopes of the different linear ion yield fits can be seen on the right hand side. (Lab.Book: 26.04.2018)

such a doubly logarithmic plot is shown. In figure 3.30(a) the pump laser power was varied, in (b) the probe laser power was varied. The ion counts were measured at 2 ps and 292 ps time delay. The slopes were obtained by performing linear fits of the data points. The slopes for the In^+, In^+He_n and the In_2^+ yields can be seen on the right side of the figure. Almost all slopes are one when rounded to the nearest whole number. The slope corresponding to the In^+ yield for variation of the probe laser power at short time delay is about 3. However, only three data points contributed to the fit, because for a very low probe laser power no In^+ ions were detected, and the result is not trustworthy. The In and In-He_n yield at 345 nm excitation clearly show larger slopes than one. It can be that at large pump and probe laser powers saturation effects occur. The probe power scan is to be repeated with a smaller step size between the data points.

3.6.1 Exciplex oscillation

Transient mass spectra were also measured with fine time steps to resolve WP oscillations. It was found that at short pump probe time delays there are WP oscillations also in the exciplex and In monomer yield. These oscillations must stem from fragmented dimers. The oscillations in the transient mass spectrum can be seen in figure 3.31 on the left. On the right, the FT is shown of the mass interval depicted in the mass spectrum. The vertical line indicates the oscillation frequency of 2.42 THz measured in the PE spectrum at 345 nm excitation wavelength (see figure 3.4). The oscillation frequency of the exciplexes

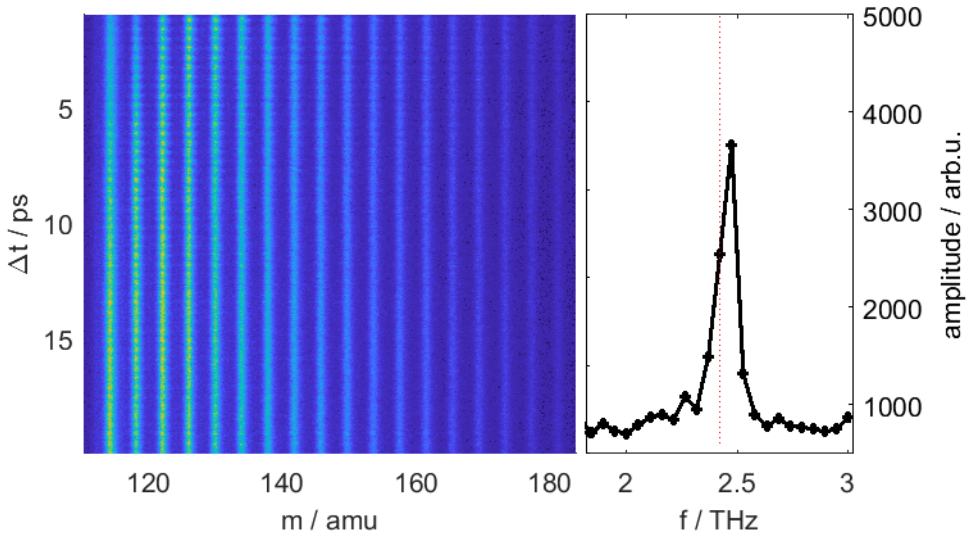

Figure 3.31: Transient mass spectrum (left) and FT (right) of coherent WP oscillations at 345 nm pump wavelength, 407 nm probe wavelength obtained with a 1 mm BBO crystal, 15 K nozzle temperature, 25 fs step size. The red dotted lines in the Fourier spectrum indicates the frequency of 2.42 THz. (Lab.Book: 25.04.2018)

is a little bit higher. The maximum in the FT spectrum lies at 2.45 THz. The result of the SWFT analysis of the oscillating exciplexes can be seen in figure 3.32. The oscillation decreases within about 15 ps and does not seem to shift.

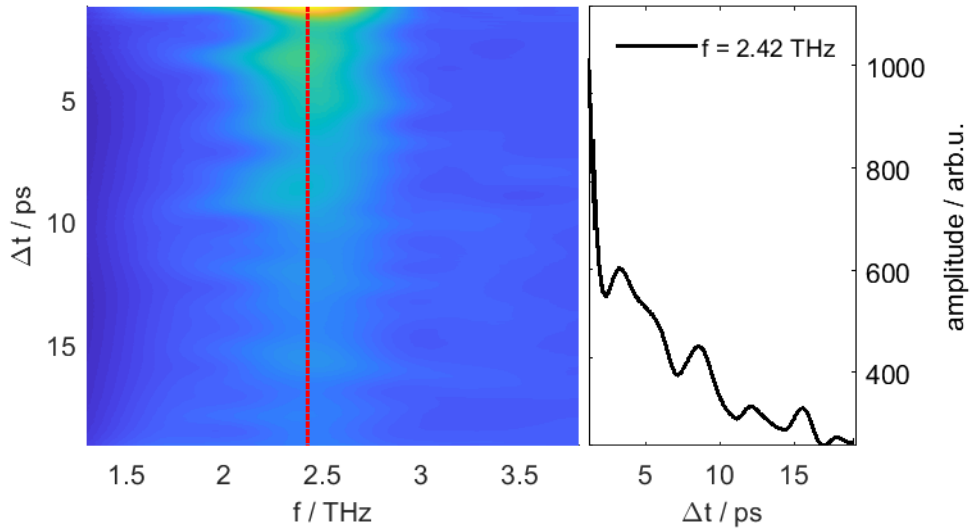

Figure 3.32: Left: SWFT of the transient mass spectrum shown in figure 3.31, with a window size of 2.5 ps. Right: Cut through the spectrogram at 2.42 THz, indicated on the left by the red vertical line.

A transient mass spectrum was also recorded in the pump-probe time regime in which the FR is expected (see figure 3.33), however, no oscillations in the exciplexes were observed. The small peak in the FT of the transient mass spectrum stems from oscillations in the In monomer yield.

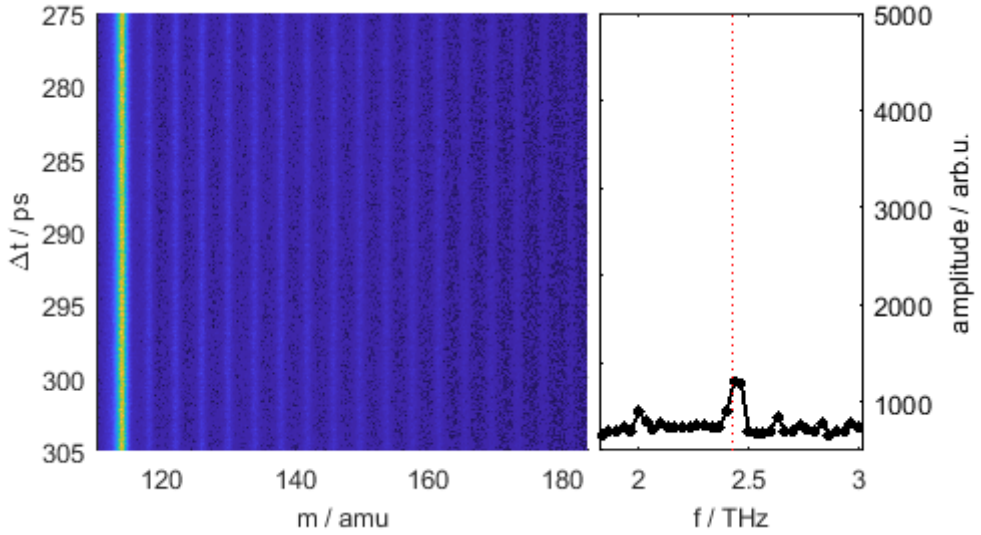

Figure 3.33: Transient mass spectrum (left) and FT (right) of In-He_n yield in the range of the pump-probe time delay where the FR is expected for excitation at 345 nm pump wavelength, 407 nm probe wavelength obtained with a 1 mm BBO crystal, 15 K nozzle temperature, 25 fs step size. No oscillations are observed in the exciplexes. The small peak in the Fourier spectrum corresponds to oscillation of the In monomer yield. The red dotted line in the Fourier spectrum indicates the frequency of 2.42 THz. (Lab.Book: 25.04.2018)

CHAPTER 4

The Wave Packet in a Morse Potential

In order to get a deeper insight into the vibrational dynamics of a diatomic molecule, a basic wave packet simulation is presented. A diatomic molecule can be approximately described by a Morse oscillator. Because this is a quite simple model it was the model of choice for the simulations, which have been carried out using Matlab. This chapter will give an overview of the Morse potential, a little review of some quantum mechanics as well as the results from the simulation. The simulation was done for In_2. The Morse parameters for the calculations were taken from [42] for the $X\ ^3\Pi_u$ ground state and the $B\ ^3\Pi_g(II)$ excited state. The source code for the simulation is listed in the appendix. There is also an open source Matlab package for the simulation of WPs. It is called WavePacket and shall be used for future simulations. For more information on it see reference [53].

4.1 The Morse Potential and its Vibrational Eigenstates

The formula for the Morse potential was first proposed in 1929 by Philipp M. Morse [54], after who the potential is named. The shape of the potential is determined by only three parameters: the equilibrium internuclear distance r_e, the dissociation energy D_e, and the fundamental frequency ω_e. The simple formula describes the potential energy of a diatomic molecule as a function of internuclear distance and looks like this:

$$V(r) = D_e(1 - e^{-\beta(r-r_e)})^2 \tag{4.1}$$

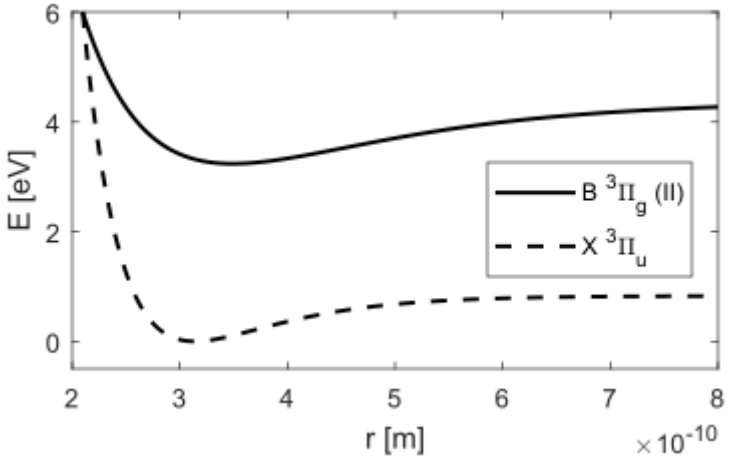

Figure 4.1: Morse potentials for In_2 of the electronic ground state (dashed line) and an electronic excited state (full line). For the Morse parameters see table 4.1.

with $\beta = \omega_e \sqrt{\frac{\mu}{2D_e}}$, and μ being the reduced mass of the molecule. The Morse potential curves of the electronic ground state (X $^3\Pi_u$) as well as of the electronic excited state (B $^3\Pi_g$ (II)), which has been identified in the experiment [50], are shown in figure 4.1. The Morse parameters to calculate the potential energy curves are listed in table 4.1.

Table 4.1: Morse potential parameters for In_2 [42]: Transition energy T_e, equilibrium distance r_e, fundamental frequency ω_e, dissociation energy D_e.

	X $^3\Pi_u$ ground state	**B $^3\Pi_g$(II) excited state**
T_e / cm^{-1}	0	26 104
r_e / Å	3.14	3.49
ω_e / cm^{-1}	111	70
D_e / eV	0.83	1.14

Within each electronic energy state there are many vibrational energy states that can be described as vibrational eigenfunctions of the Morse oscillator. An analytic solution to the Schrödinger equation was proposed by Morse [54]. An adapted form of the original analytical solution was taken from reference [55] for the simulation. The eigenvalues of the vibrational states were calculated with the following formula, where n represents the vibrational quantum number.

$$E_n = \hbar\omega_e(n + 1/2) - \frac{[\hbar\omega_e(n + 1/2)]^2}{4D_e} \tag{4.2}$$

The first term yields the equidistant energy values that are known from the vibrational levels of the harmonic oscillator. The latter term brings the anharmonicity of the Morse potential into play. It can be seen that for increasing n the spacing between two adjacent

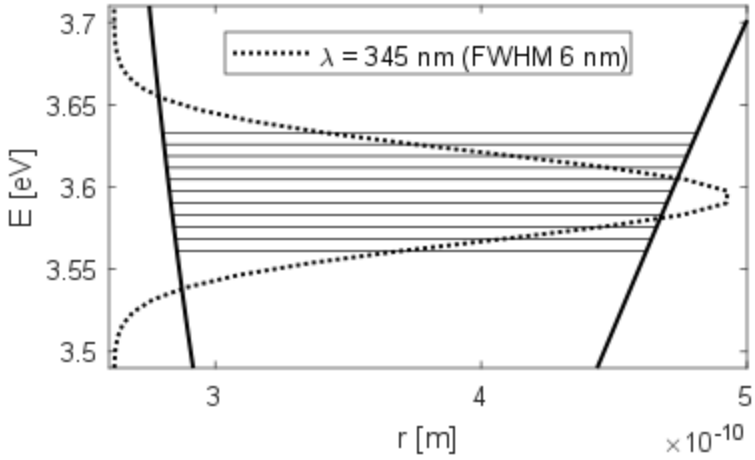

Figure 4.2: Zoom into the excited B-state Morse potential curve (thick full line) to compare the spectral width of the pump pulse (dotted line, excitation energy 345 nm $\hat{=}$ 3.59 eV) with the energetic spacing of vibrational eigenstates (thin horizontal lines).

energy levels decreases. Excitation of vibrational levels that lie high within the Morse potential will have a smaller spacing between the energy levels, which subsequently leads to a lower vibrational frequency of the wave packet. This can easily be observed with this simulation.

To demonstrate the results of the simulation an excitation wavelength of 345 nm (3.59 eV) with a spectral width of 6 nm FWHM was chosen. Figure 4.2 shows a small section of the Morse potential of the excited B state, the vibrational energy levels from $n = 41$ to $n = 51$, as well as a Gaussian profile that represents our excitation laser pulse. The spectral width of the pump pulse is well large enough to coherently excite several vibrational states.

The analytical solution for the vibrational eigenstates that was used to realise the simulation is shown in here [55]:

$$\Psi_n(z) = N_n z^{\lambda-n-1/2} e^{-1/2z} L_n^{2\lambda-2n-1}(z) \tag{4.3}$$

$L_n^{(\alpha)}$ represents a generalised Laguerre polynomial of degree α for the n^{th} eigenstate. Also, some new variables have been introduced in order to obtain this compact form of the eigenstates:

$$N_n = \left[\frac{n!(2\lambda-2n-1)}{\Gamma(2\lambda-n)}\right]^{1/2} \qquad z = 2\lambda e^{-(x-x_e)}$$
$$x = \beta r \tag{4.4}$$
$$\lambda = \frac{\sqrt{2\mu D_e}}{\beta\hbar} \qquad x_e = \beta r_e$$

The parameter β is the same that was introduced above to calculate the Morse potential.

Γ stands for the Gamma function.

4.2 Temporal Evolution of a Vibrational Wave Packet

The vibrational eigenfunctions of the Morse potential are now known. To better understand how the wave packet was created and how its temporal evolution was calculated in the simulation, a little reminder of some basic quantum mechanics is given here.

We start off with the time dependent Schroedinger equation:

$$H|\Psi_n(t)\rangle = E_n|\Psi_n(t)\rangle = i\hbar\frac{\partial|\Psi_n(t)\rangle}{\partial t} \tag{4.5}$$

When the Hamiltonian of the system is not explicitly time dependent, as it is the case here, the time dependence of the eigenstate $|\Psi_n(t)\rangle$ can be written as an exponential prefactor, the time dependent phase $\phi(t)$ of the eigenstate.

$$|\Psi_n(t)\rangle = e^{-i\phi(t)}|\Psi_n\rangle = e^{-iE_nt/\hbar}|\Psi_n\rangle \tag{4.6}$$

with $|\Psi_n\rangle$ being the stationary eigenstate of the Morse oscillator and E_n the eigenvalue, which are calculated with the formulas 4.2 and 4.3. A state $|\Psi(t)\rangle$, which is not an eigenstate, can be written as a superposition of eigenstates.

$$|\Psi(t)\rangle = \sum_n a_n|\Psi_n(t)\rangle \tag{4.7}$$

In the above equation a_n is a normalised weight factor ($\sum_n |a_n|^2 = 1$) that describes which eigenstates n are populated and how strongly they are populated. For the simulation a Gaussian distribution of the weight factors was chosen, corresponding to the Gaussian spectral profile of the excitation laser pulse (see figure 4.2). To calculate the temporal evolution of a superposition of eigenstates, the time dependent phase can be combined with the weight factor a_n as follows:

$$|\Psi(t)\rangle = \sum_n a_n e^{-iE_nt/\hbar}|\Psi_n\rangle = \sum_n a_n(t)|\Psi_n\rangle \tag{4.8}$$

This was simply done to reduce the computational effort, because in this way it was possible to calculate the stationary eigenstates only once and later on multiply any weight factor and time dependence to create a specific wave packet. How the Gaussian weight factors were calculated can be seen in listing 6.2 in the appendix.

In order to include the transition probability from the ground state to an excited state, the Franck-Condon factors have to be calculated. The Franck-Condon integral represents the spatial overlap of the respective wave functions of the initial and the final state. It is based on the Born-Oppenheimer principle, namely that nuclear motion happens much slower than electronic excitation, so that the internuclear distance stays the same during the excitation process.

$$a_{FC} = \int \Psi_i^* \Psi_f dr \tag{4.9}$$

Here Ψ_i and Ψ_f represent the initial and the final state. The initial state is in this case always the electronic ground state with the vibrational quantum number $n = 0$, the final state represents the electronic excited state for different quantum numbers n. To calculate the temporal evolution of the WP the Franck-Condon factors for the different states are multiplied with the Gaussian weight factors a_n (see appendix, listing 6.2) and subsequently normalised.

In figure 4.3 the simulated WP is shown at the time of its creation. It shall be noted that all eigenstates start off with zero phase ($\phi(t = 0) = 0$). On the left, vibrational eigenfunctions were weighed with Gaussian weights, the WP is localised at the outer turning point of the potential. Including the FC factors in the calculation yields a WP that is initially located at the inner turning point of the potential (figure 4.3 on the right), because the equilibrium distance of the ground state lies at a smaller internuclear distance and therefore there is a larger FC overlap at smaller distances.

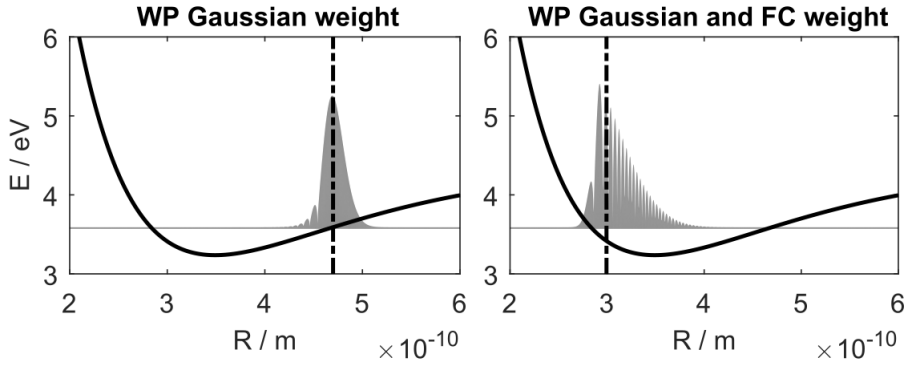

Figure 4.3: Vibrational WP at time zero (time delay $\Delta t = 0\,ps$), when all eigenstates have zero phase. Full line: Excited state Morse potential. Dashed line: expectation value of position operator. Grey shaded area: absolute value of the wave function of the WP. On the left the eigenfunctions constituting the WP have been weighed with Gaussian weights only. On the right the Franck-Condon overlap has additionally been included in the weight factors.

Table 4.2 lists the weight factors for the population of the vibrational states, whose superposition result in the WPs shown in figure 4.3. It can be seen that for a purely Gaussian

Table 4.2: WP weight factors: Vibrational quantum numbers n, purely Gaussian weight factors a_{gauss}, weight factors including FC overlap $a_{gauss,\ FC}$.

n	$\mathbf{a_{gauss}}$	$\mathbf{a_{gauss,\ FC}}$
33	2.3016e-3	1.5852e-1
34	5.5035e-3	2.7620e-1
35	1.2095e-2	3.9386e-1
36	2.4459e-2	4.6545e-1
37	4.5558e-2	4.4971e-1
38	7.8243e-2	3.3556e-1
39	1.2403e-1	1.5371e-1
40	1.8166e-1	3.6369e-2
41	2.4610e-1	1.7653e-1
42	3.0868e-1	2.3719e-1
43	3.5885e-1	2.2499e-1
44	3.8704e-1	1.7010e-1
45	3.8769e-1	1.0578e-1
46	3.6103e-1	5.3830e-2
47	3.1287e-1	2.1320e-2
48	2.5257e-1	5.3329e-3
49	1.9012e-1	4.7622e-4
50	1.3358e-1	1.5690e-3
51	8.7686e-2	1.1579e-3

weight, higher states (from about $n = 39$ to $n = 50$) are populated more strongly than when the FC overlap is included in the weight factor. The FC factors lead to more population in states around the vibrational quantum number $n = 36$, fewer population around $n = 40$ and again some more population in $n = 42$ and 41.

To investigate the temporal evolution of the WP, the expectation value of the position operator was calculated. Again, the stationary eigenstates were used to calculate the matrix elements of the position operator $\hat{X}$ and the position matrix was afterwards multiplied with the time dependent weight factors:

$$X_{mn} = \langle \Psi_m | \hat{X} | \Psi_n \rangle \tag{4.10}$$

$$\langle X(t) \rangle = \sum_{m,n} a_m^*(t) X_{mn} a_n(t) \tag{4.11}$$

The temporal evolution of the expectation value of the position operator can be seen in figure 4.4 up to half of the revival time $T_{rev}/2$. On the left the result for the simulation with Gaussian weight factors is shown, while for the result shown on the right, the FC overlap has been included in the calculations. It can be immediately seen that the

revival time is the same for both WPs, since it only depends on the anharmonicity of the potential. The revival time was calculated with formula 1.1 to be 250 ps. Also the $1/4^{\text{th}}$ revival (at about 60 ps time delay) appears at the same time after creation of the WP. However, when the FC overlap is included, the $1/6^{\text{th}}$ revival (at about 40 ps time delay) is not visible in the graph. It can also be seen that for purely Gaussian weights the oscillation of the expectation value drops to half its initial value after about 10 ps, while this takes about twice as long when the FC overlap is included in the simulation. This already indicates that to accurately describe the experimental findings a more sophisticated simulation model is necessary.

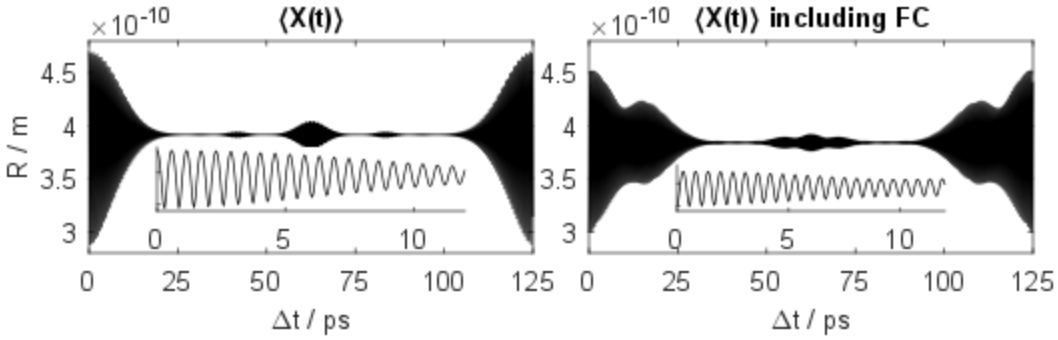

Figure 4.4: Expectation value of the position operator as a function of time. Left: Expectation value calculated from solely Gaussian weight factors. Right: FC overlap was included in the calculation. In the insets on the left and right the first few picosecons are shown to make the oscillations visible.

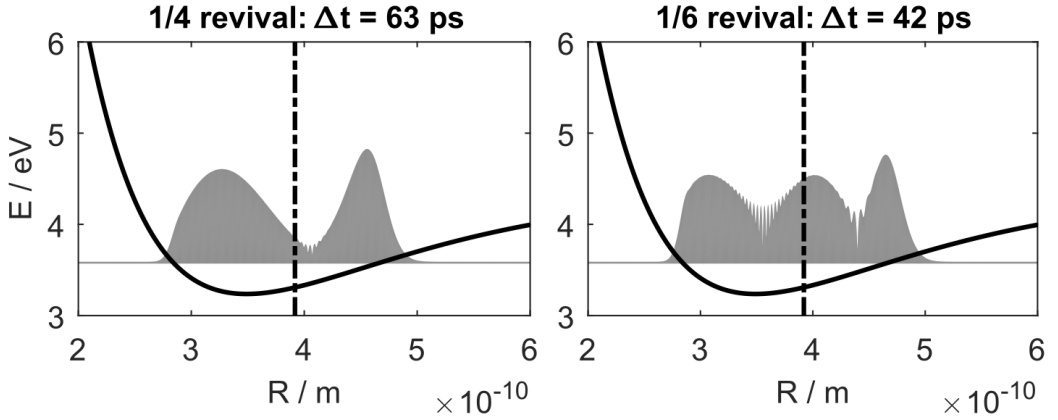

Figure 4.5: Fractional revivals: On the left a quarter revival with two localised features is shown. A $1/6^{\text{th}}$ revival with three localised features can be seen on the right.

To estimate the oscillation frequency of the WP the oscillation frequency of two neighbouring states can be calculated from the energy difference between these two vibrational

states. This frequency is calculated in the following way:

$$f(\Delta E) = \frac{\Delta E}{h}$$

with $\Delta E = E_{n+1} - E_n$ being the energy difference of the two adjacent vibrational eigenstates $n+1$ and n. Coupling of the states $n = 45$ and $n = 46$ for example leads to an oscillation frequency of about 1.73 THz of the WP.

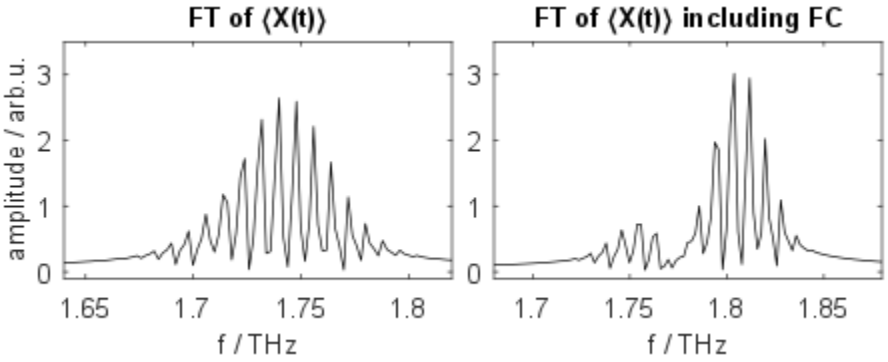

Figure 4.6: Frequency spectra of the simulated WPs obtained via Fourier transformation of the temporal evolution of the position operator expectation values shown in figure 4.4.

Another method to obtain the oscillation frequency of the simulated WP is to perform a Fourier transform of the temporal evolution of the expectation value of the position operator. The result of this Fourier transformation is shown in figure 4.6. It can be seen that the WP oscillates at several different frequencies, which correspond to the different vibrational eigenstates of which the WP consists. When the FC overlap is included in the simulation the WP oscillates at slightly higher frequencies. From this it can be inferred that lower vibrational states are populated. The gap in the frequency spectrum illustrates a small FC overlap between the ground state and respective excited vibrational states. This reflects very well how strongly the different vibrational states are populated, corresponding to the weight factors listed in table 4.2. In the frequency spectrum also two and three times the fundamental frequencies, corresponding to the $1/4^{\text{th}}$ and $1/6^{\text{th}}$ revival, can be seen, but with small amplitudes, however, these are not shown here.

Comparing the results from the simulation to the experimental results, it is found that the simulated WP oscillates at lower frequencies ($\sim$1.74 THz without and $\sim$1.80 THz with FC overlap) than the In_2 in the experiment ($\sim$2.4 THz at 345 nm excitation wavelength). Only excitation at 365 nm yielded a comparable experimental oscillation frequency of $\sim$1.80 THz. The revival time of 290 ps found in the experiment also exceeds the calcu-

lated revival time of 250 ps. These different results most likely arise from a difference in the anharmonicity between the actual diatomic potential in the He droplet and the approximated Morse potential used in the simulation. The potential energy curve of the In_2 could be distorted due to the surrounding He. The higher vibrational frequency in the experiment could hint at larger energy gaps between two adjacent vibrational levels. From the larger experimental revival time it can be presumed that the actual form of the potential is more harmonic than the Morse potential. For I_2 in solid Kr it was found that the excited state within the cage showed a smaller anharmonicity compared to the free molecule [13].

CHAPTER 5

Outlook

The results obtained within the course of this master's thesis represent a proof-of-concept that coherent molecular dynamics of species immersed in superfluid He_N can be observed with ultrafast laser spectroscopy on its natural time scale. It has been shown that coherence is, at least to some extent, maintained throughout the bubble expansion and dopant ejection process triggered by photoexcitation of the molecule. These findings open up the way for a whole new range of experiments. However, some open questions remain and further experiments and simulations regarding the characterisation of WPs in a diatomic molecule should be undertaken, in order to get a deeper understanding of the processes that are taking place.

Some questions that arose from the experimental observations of In_2 in He_N and are yet unanswered are the following:

- The transient PE spectra obtained at photoexcitation with 345 nm shows three features.
  What state can the higher energy peak, that decreases with increasing pump-probe time delay, be assigned to?
  Which PE signal corresponds to the detected exciplexes?
  Where does the signal toward lower PE energies stem from? Could it stem from ionization to a higher lying ionic state?
- To what excited state of In_2 can the excitation band around 365 nm be assigned?
- How are the $InHe_n$ exciplexes formed and why can no revival of the WP be observed?

Characterisation measurements concerning the In_2 inside He_N WP

- Perform a systematic variation of pump and probe wavelength.
  By varying the excitation wavelength one can investigate how the oscillation frequency of the primary WP oscillations, the HR and the FR, as well, as the revival time change with the amount of energy that is initially put into the system.
  When the outer turning point of the potential energy curve is determined one can map the potential curve by simultaneous variation of the pump and the probe wavelength. The wavelengths have to be varied simultaneously in order to always be within a Franck-Condon window at different internuclear distances.

- Measure the 3/2-revival of the In_2 WP.
  By the time the WP refocuses at the FR, all In_2 molecules have been ejected from the He droplet. The time between the FR and the 3/2-revival, which is expected at 435 ps after photoexcitation, represents the revival time of free In_2. If this differs from the revival time measured between the primary oscillations and the HR or between the HR and the FR, respectively, information on the deformation of the potential energy curve by the He droplet can be gained.

Simulations concerning the the In_2 inside He_N WP

- Include decoherence, dissipation and dopant ejection in the WP simulation. To accurately simulate the experimental PE and photoion yield, it has to be taken into account how the He surrounding affects the WP oscillations. The most prominent effect that is missing in the simulation so far is decoherence. The oscillation amplitudes of the measured WP revivals are significantly smaller than the primary oscillations due to a loss of phase relation between the different vibrational states. Ejection of the dopant from the He_N

- It would be a great advantage for the interpretation of the experimental findings if a calculation of the In_2-He potential energy surfaces of the electronic ground, excited and ionic state could be had.

Experiments concerning other systems

- Dope He_N with lighter diatomic molecules. It could be investigated if the oscillation of smaller masses couples more strongly to the surrounding He bath and if therefore stronger or faster decoherence during the dopant-He interaction process is observed.
- It would be interesting to observe photoinduced molecule association. He_N could be doped with atoms that are known to reside in separate He solvation shells, or one is located in the interior of the droplet, another located at the droplet surface. Can a coherent signal be observed after a molecule formation process? On what time scales does the formation process occur when a He barrier has to be overcome?
- Co-dope for example In_2 in He_N with other molecules and investigate how their presence affects the WP oscillation and coherence properties.

CHAPTER 6

Appendix

A Sliding Window Fourier Transformation

The transient electron spectra, in which the vibrational wave packet oscillations were measured, were analysed using Sliding Window Fourier Transformation (SWFT). The basic idea of this method is to choose a certain temporal part of the whole measurement (as if viewed through a narrow time window) and do a Fourier transform (FT) of this part. A typical window comprises about 100 time points, however, the size does depend on the length of the measurement and the frequencies one wants to resolve. Then the window will be moved step by step across the whole signal and FTs are calculated at each position of the window. This is done in order to see when and if certain frequencies appear and/or disappear throughout the measurement. To understand this technique a step by step explanation of the analysis is given here. Also, the Matlab code written by Pascal Heim used for the analysis is listed.

A.1 Introduction to SWFT

Figure 6.1 shows a transient electron spectrum as the ones in chapter 3. The first step is to do a FT for each energy, which corresponds to a FT of each row of the spectrum. This was done using the Fast Fourier Transform (FFT) function provided by Matlab. Matlab returns the frequency spectrum in such a way that the maximum frequency lies in the middle of the returned vector, as can be seen in a schematic example of a frequency spectrum on the left side in figure 6.2. To display the frequencies in a more intuitive way,

the frequency spectrum was reshaped so that the maximum frequency appears at the end of the spectrum, see figure 6.2 on the right.

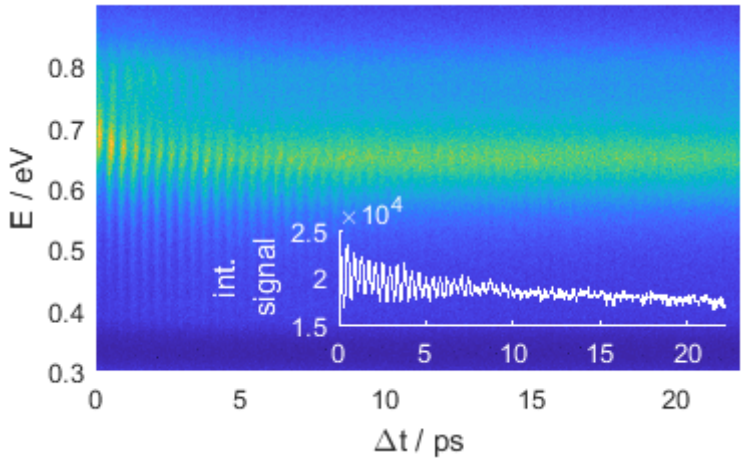

Figure 6.1: Transient PE spectrum. Inset: Integrated PE signal shows oscillations on top of positive 'background' signal. (Lab.Book: 18.04.2018)

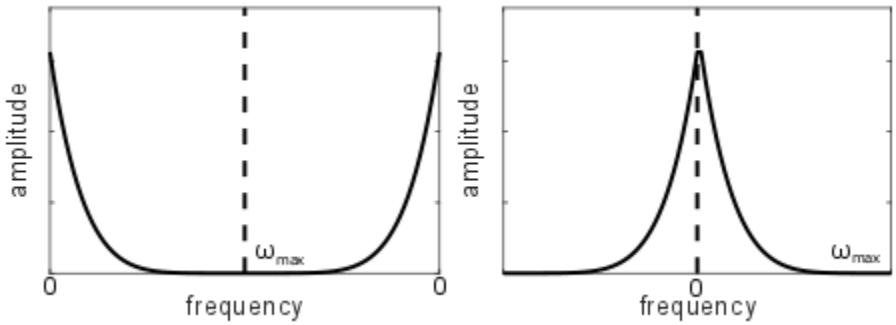

Figure 6.2: Left: Schematic frequency spectrum obtained with Matlab FFT function. Right: Reshaped schematic frequency spectrum for more intuitive display.

Summing up the absolute value of the reshaped FTs of all different PE energies results in the frequency spectrum shown in figure 6.3. The very high peak that appears around 0 THz is due to the finite length of the measurement, and because the signal does not oscillate around zero, but around a 'positive offset', which can be seen in the integrated PE signal (inset in figure 6.1). There is no information within the 0 THz-peak. In order to omit the contribution of these low frequencies in the analysis, a spectral filter is applied, meaning that frequencies below a certain threshold are set to zero. The threshold is indicated in figure 6.3 by dashed vertical lines.

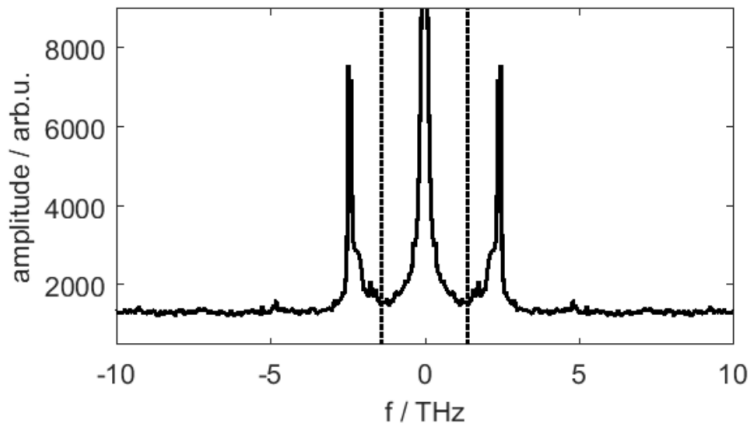

Figure 6.3: Fourier transform of the whole measurement: Frequencies below a certain threshold (dashed vertical lines) are set to zero.

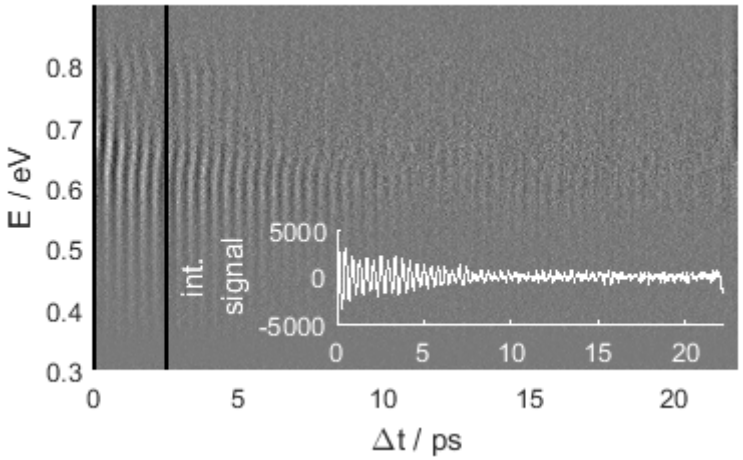

Figure 6.4: Modified PE spectrum obtained through inverse Fourier transformation of frequency the spectrum after filtering low frequencies. Inset: Integrated signal oscillates around zero. Red vertical lines indicate window size for SWFT.

The next step in the analysis is to do an inverse Fourier transformation of the spectrally filtered frequency spectra. Filtering of the low frequencies leads to the modified PE spectrum shown in figure 6.4. As can be seen in the inset, the integrated signal now oscillates around zero.

For the analysis in this work a window size of 100 time points was chosen, which corresponds in our case to a time window of 2.5 ps. The window size is indicated in figure 6.4 by two vertical red lines. One can choose from many different window functions, the simplest one being a rectangle. For the analysis here a Hamming window was used as the window function, which is defined by the equation 6.1. The N in the equation stands for the window size, $N = 100$ in our case, and n is the running index. The Hamming window function as well as its FT are depicted in figure 6.5.

$$W(n) = \frac{25}{46} - \frac{21}{46} * \cos\left(\frac{2\pi * n}{\mathrm{N}}\right) \tag{6.1}$$

The signal that lies within the chosen window is then pointwise multiplied with the window function. A simple trick to improve the FT resolution is called "zero padding", which means that trailing zeros are added to the windowed signal. It is useful to choose the number of added zeros so that the total number of points (windowed signal plus trailing zeros) equals a power of 2. This makes the FFT algorithm somewhat faster. We used a total number of 512 points for the analysis here.

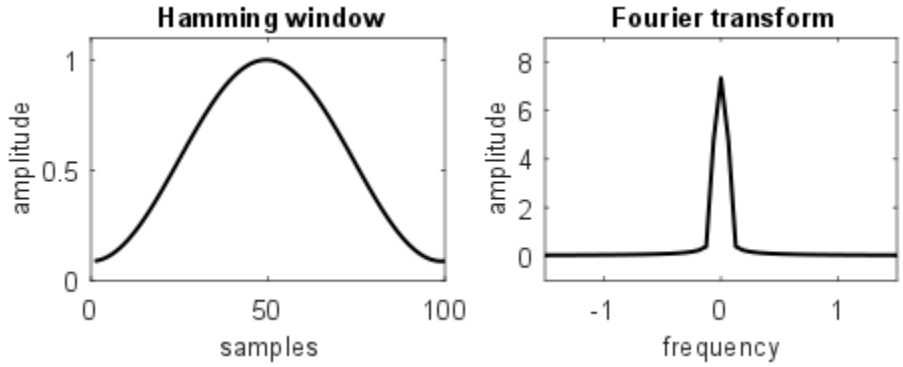

Figure 6.5: Hamming window function for $N = 100$ points and its corresponding FT

After the SWFT analysis has been applied to the modified PE spectrum the result is a three dimensional array, namely frequency spectra over time for all the different PE energies. To finally obtain a sliding window Fourier spectrum as the one in figure 6.6, the absolute values of the frequency spectra are summed up over all PE energies.

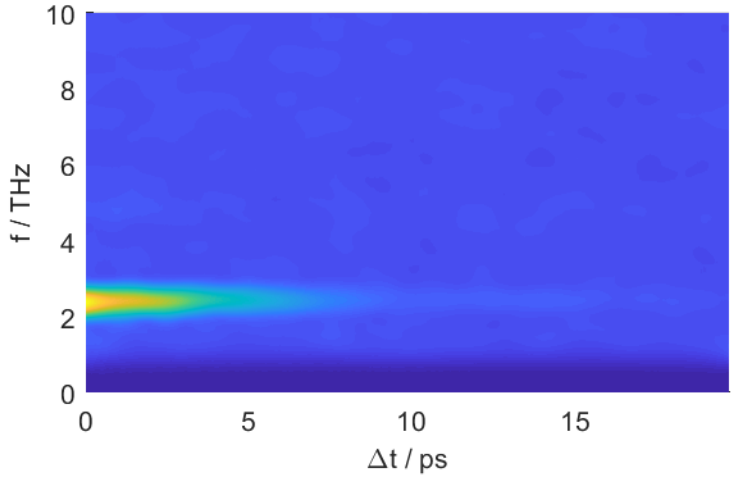

[h!]

Figure 6.6: Sliding window Fourier spectrum: Only positive frequencies are shown, because the frequency spectrum is fully symmetric.

A.2 SWFT Matlab Code

fft, *ifft*, *fftshift* and *ifftshift* are predefined Matlab functions. fft_spec is a modified version of Matlab's *fft* that gives out the reshaped frequency spectrum as well as the angular frequency calculated from the time steps. The threshold frequency for the spectral filter has to be given in terahertz.

Listing 6.1: Matlab code for SWFT analysis of transient PE spectra

```
1
2 % Fourier Transformation
3 function [w, y_fft] = fft_spec(t, y, dim, N)
4     if nargin < 4
5         N = numel(t);
6     end
7     N = max(N,numel(t));
8     dt = abs(t(2)-t(1));
9     y_fft = fftshift(fft(y, N, dim), dim)*dt;
10
11    w = mod(2*pi*(0:(N-1))/N+pi, 2*pi) - pi;
12    w = fftshift(w/dt);
13 end
14
15 % apply spectral filter
16 spectralFilter = (abs(w) > f_threshold*2*pi).';
17 for i = 1:size(y_fft,2)
18     y_fft(:,i) = y_fft(:,i).*spectralFilter;
19 end
20
21 % inverse Fourier Transormation of filtered frequency spectrum
22 h = ifft(ifftshift(y_fft/(t(2)-t(1)),1),[],1);
23
24 % Sliding Window Fourier Transform
```

```
25 [w, t_new, h_fft_sliding] = ...
26     sliding_fft(t, h, windowSizeTimepoints,512,'hamming');
27
28 function [w, t_new, y_fft_sliding] = ...
29         sliding_fft(t, y, windowSizeTimepoints, N, windowfkt)
30     if nargin < 4
31         N = windowSizeTimepoints;
32     end
33     if nargin < 5
34         windowfkt = 'rectangle';
35     end
36     N = max(N, windowSizeTimepoints);
37
38     t_new = t(1:(end-windowSizeTimepoints));
39     y_fft_sliding = nan([N, size(y,2), numel(t_new)]);
40
41     switch windowfkt
42         case 'rectangle'
43             windowfkt = 1;
44         case 'hamming'
45             windowfkt = repmat(...
46                 hammingWindow(windowSizeTimepoints).',[1,size(y,2)]);
47         otherwise
48             windowfkt = 1;
49     end
50
51     for i = 1:numel(t_new)
52         ind = (1:windowSizeTimepoints)+i;
53         [w, y_fft_sliding(:,:,i)] = ...
54          fft_spec(t(ind), windowfkt.*y(ind,:), 1,N);
55     end
56
57 end
58
59 % Hamming window
60 function w = hammingWindow(N)
61     w = 25/46 - 21/46*cos(2*pi*(1:N)/(N));
62 end
63
64 % sum of over all PE energies
65 h_fft_sliding_abs = squeeze(nansum(abs(h_fft_sliding), 2));
```

B WP Simulation

Morse potential parameters for the simulation were taken from reference [42] and are listed in table 4.1. Physical constants were used in different units in the simulation. For clarification, physical constants and the atomic mass of In used in the simulation are listed in table 6.1.

In the wave packet simulation n represents the vibrational quantum number. Eigenstates

were calculated up to n = 91. For higher quantum numbers the eigenstates were not normalised anymore, which was probably due to computational errors.

Table 6.1: Physical constants and atomic mass of In

Name of variable in simulation	Physical constant	Unit	Value
c	c	cm/s	2.99792458e10
cSI	c	m/s	2.99792458e8
h	h	eV s	4.135667662e-15
hSI	h	m^2kg/s	6.62607004e-34
u	u	kg	1.660539040e-27
mass		u	114.818

Listing 6.2: Matlab code for WP simulation

```
%%% Calculate vibrational eigenstates and position operator matrix

%reduced mass
mu = mass*u/2;

reSI = re*10^(-10);
veSI = we*c;
DeSI = De*1.6021766208e-19;

rSI = linspace(2e-10,12e-10,3000);

beta = pi*veSI*sqrt(2*mu/DeSI);
x = beta*rSI;
xe = beta*reSI;
lam = sqrt(2*mu*DeSI)/(beta*hSI/(2*pi));

% Vibrational quantum numbers
n  = [0:91];

lnNn = gammaln(n+1) + log(2*lam-2*n-1) - gammaln(2*lam-n);
z = 2*lam*exp(-(x-xe));
alpha = 2*lam-2*n-1;

% vibrational eigenenergies
EnSI = hSI*veSI*(n+1/2) - (hSI*veSI*(n+1/2)).^2/(4*DeSI);

% Vibrational eigenstates
Psi_nX = zeros(numel(n),numel(z));
for i = 1:numel(n)
    Psi_nX(i,1:end) = exp(1/2*lnNn(i) + (lam-n(i)-1/2)*log(z) - ...
      1/2*z + log(laguerreL(n(i),alpha(i),z)));
end
Psi_n = Psi_nX.*sqrt(beta);

% position operator matrix elements <Psi_m|X|Psi_n>
Xmn = zeros(numel(n),numel(n));
```

```
for i = 1:size(Xmn,1)
    Xmn(i,i) = sum(conj(Psi_n(i,1:end)).*rSI.*...
      Psi_n(i,1:end).*(rSI(2)-rSI(1)));
end
for i = 2:size(Xmn,1)
    for k = 1:(i-1)
        Xmn(i,k) = sum(conj(Psi_n(i,1:end)).*rSI.*...
          Psi_n(k,1:end).*(rSI(2)-rSI(1)));
        Xmn(k,i) = conj(Xmn(i,k));
    end
end

%%% Create wave packet
% set parameters:
% => transition energy
% => pump laser wavelength
% => spectral width of pump laser

% Transition energy
Te = 26104;
TeSI = Te*c*hSI;

% Pump laser
lambda = 345e-9;    % wavelength
delta_lambda = 6e-9;    % FWHM

Epump = hSI*cSI/lambda;
delta_Epump = delta_lambda/lambda*Epump;
sigma = delta_Epump/(2*sqrt(2*log(2)));

EWP = Epump-TeSI;

% Gaussian weights to populate eigenstates
a = 1/(sigma*sqrt(2*pi))*exp(-1/2*((EnSI-EWP)/sigma).^2);
a = a/sqrt(sum(abs(a).^2));

% Franck-Condon factors
aFC = conj(Psi_n)*Psi_ground.'*(rSI(2)-rSI(1));

% Gaussian and Franck-Condon weight
a_tot = a.*aFC.';
a_tot = a_tot/sqrt(sum(abs(a_tot).^2)); %normalise


% t       time / s after creation of wave packet
% at      time dependent Gaussian weights
% WP      wave function of wave packet at time t
% expVal Expectation value of position operator at time t
t = 0e-12;
at = a.*exp(-1i*EnSI*t/(hSI/(2*pi))); % without FC overlap
% at = a_tot.*exp(-1i*EnSI*t/(hSI/(2*pi))); % with FC overlap
WP = zeros(size(rSI));
for i = 1:numel(a)
    atPsi = at(i).*Psi_n(i,1:end);
```

```
91      WP = WP + atPsi;
92  end
93  expval = at*Xmn*at';
```

Bibliography

[1] Carlo Callegari and Wolfgang Ernst. "Helium Droplets as Nanocryostats for Molecular Spectroscopy - from the Vacuum Ultraviolet to the Microwave Regime". In: *Handbook of High-Resolution Spectroscopy*. Ed. by Martin Quack and Merkt Frédéric. 1st ed. Vol. 3. John Wiley & Sons, 2011, pp. 1551–1594. URL: https://doi.org/10.1002/9780470749593.hrs064.

[2] J Peter Toennies and Andrey F Vilesov. "Superfluid helium droplets: a uniquely cold nanomatrix for molecules and molecular complexes". In: *Angewandte Chemie International Edition* 43 (2004), pp. 2622–2648. URL: https://doi.org/10.1002/anie.200300611.

[3] M Hartmann et al. "Rotationally resolved spectroscopy of SF_6 in liquid helium clusters: A Mmlecular probe of cluster temperature". In: *Physical Review Letters* 75 (1995), p. 1566. URL: https://doi.org/10.1103/PhysRevLett.75.1566.

[4] John Higgins et al. "Photoinduced chemical dynamics of high-spin alkali trimers". In: *Science* 273 (1996), pp. 629–631. DOI: 10.1126/science.273.5275.629.

[5] Anna Gutberlet et al. "Aggregation-induced dissociation of HCl $(H_2O)_4$ below 1 K: The smallest droplet of acid". In: *Science* 324 (2009), pp. 1545–1548. DOI: 10.1126/science.1171753.

[6] Ahmed H Zewail. "The new age of structural dynamics". In: *Acta Crystallographica Section A* 66 (2010), pp. 135–136. URL: https://doi.org/10.1107/S0108767309047801.

[7] Michael P Ziemkiewicz, Daniel M Neumark, and Oliver Gessner. "Ultrafast electronic dynamics in helium nanodroplets". In: *International Reviews in Physical Chemistry* 34 (2015), pp. 239–267.

[8] M. Mudrich and F. Stienkemeier. "Photoionisaton of pure and doped helium nanodroplets". In: *International Reviews in Physical Chemistry* 33 (2014), pp. 301–339. DOI: 10.1080/0144235X.2014.937188. eprint: https://doi.org/10.1080/

0144235X.2014.937188. URL: https://doi.org/10.1080/0144235X.2014.937188.

[9] Johannes Von Vangerow et al. "Imaging excited-state dynamics of doped He nanodroplets in real-time". In: *The Journal of Physical Chemistry Letters* 8 (2016), pp. 307–312. URL: https://pubs.acs.org/doi/abs/10.1021/acs.jpclett.6b02598.

[10] Bernhard Thaler et al. "Femtosecond photoexcitation dynamics inside a quantum solvent". In: *Nature Communications* 9 (Oct. 2018), p. 4006. ISSN: 2041-1723. URL: https://doi.org/10.1038/s41467-018-06413-9.

[11] Markus Gühr. "Coherent dynamics of small molecules in rare gas crystals". PhD thesis. Freie Universität Berlin, 2005.

[12] Ingo Fischer et al. "Femtosecond time-resolved zero kinetic energy photoelectron and photoionization spectroscopy studies of I_2 wavepacket dynamics". In: *Chemical physics* 207 (1996), pp. 331–354. URL: https://ac.els-cdn.com/0301010495004041/1-s2.0-0301010495004041-main.pdf?_tid=4c3bbae3-5097-4a31-9e75-8174fe6e0f42&acdnat=1537270635_d3e2b64a306a9c35ae253719309973e1.

[13] M Gühr et al. "Ultrafast dynamics of halogens in rare gas solids". In: *Physical Chemistry Chemical Physics* 9 (2007), pp. 779–801. DOI: 10.1039/B609058N.

[14] RM Bowman, M Dantus, and AH Zewail. "Femtosecond transition-state spectroscopy of iodine: From strongly bound to repulsive surface dynamics". In: *Chemical Physics Letters* 161 (1989), pp. 297–302. URL: https://doi.org/10.1016/0009-2614(89)85088-2.

[15] M Dantus, MHM Janssen, and AH Zewail. "Femtosecond probing of molecular dynamics by mass-spectrometry in a molecular beam". In: *Chemical physics letters* 181 (1991), pp. 281–287. URL: https://doi.org/10.1016/0009-2614(91)80071-5.

[16] M Gruebele et al. "Femtosecond temporal spectroscopy and direct inversion to the potential: Application to iodine". In: *Chemical physics letters* 166 (1990), pp. 459–469. URL: https://doi.org/10.1016/0009-2614(90)87134-D.

[17] Horia Metiu and Volker Engel. "A theoretical study of I_2 vibrational motion after excitation with an ultrashort pulse". In: *The Journal of Chemical Physics* 93 (1990), pp. 5693–5699. URL: https://doi.org/10.1063/1.459563.

[18] Qianli Liu, Chaozhi Wan, and Ahmed H Zewail. "Solvation ultrafast dynamics of reactions. 13. Theoretical and experimental studies of wave packet reaction coherence and its density dependence". In: *The Journal of Physical Chemistry* 100 (1996), pp. 18666–18682. DOI: 10.1021/jp962432v.

[19] M Karavitis and VA Apkarian. "Vibrational coherence of I_2 in solid Kr". In: *The Journal of chemical physics* 120 (2004), pp. 292–299. URL: https://doi.org/10.1063/1.1630567.

[20] Matias Bargheer, Markus Gühr, and Nikolaus Schwentner. "Collisions transfer coherence". In: *Israel journal of chemistry* 44 (2004), pp. 9–17. URL: https://doi.org/10.1560/WFHD-7VCV-877K-229N.

[21] Patrick Claas et al. "Wave packet dynamics in triplet states of Na_2 attached to helium nanodroplets". In: *The Journal of Physical Chemistry A* 111 (2007), pp. 7537–7541. DOI: 10.1021/jp070893i.

[22] M Mudrich et al. "Spectroscopy of triplet states of Rb_2 by femtosecond pump-probe photoionization of doped helium nanodroplets". In: *Physical Review A* 80 (2009), p. 042512. URL: https://doi.org/10.1103/PhysRevA.80.042512.

[23] Barbara Grüner et al. "Vibrational relaxation and dephasing of Rb_2 attached to helium nanodroplets". In: *Physical Chemistry Chemical Physics* 13 (2011), pp. 6816–6826. DOI: 10.1039/C0CP02355H.

[24] P Claas et al. "Wave packet dynamics of K_2 attached to helium nanodroplets". In: *Journal of Physics B: Atomic, Molecular and Optical Physics* 39 (2006), S1151. URL: http://iopscience.iop.org/article/10.1088/0953-4075/39/19/S23/meta.

[25] Martin Schlesinger et al. "Dissipative vibrational wave packet dynamics of alkali dimers attached to helium nanodroplets". In: *Chemical Physics Letters* 490 (2010), pp. 245–248. ISSN: 0009-2614. DOI: https://doi.org/10.1016/j.cplett.2010.03.060. URL: http://www.sciencedirect.com/science/article/pii/S0009261410004586.

[26] Martin Schlesinger and Walter T Strunz. "Detailed model study of dissipative quantum dynamics of K_2 attached to helium nanodroplets". In: *New Journal of Physics* 14 (2012), p. 013029. URL: http://iopscience.iop.org/article/10.1088/1367-2630/14/1/013029/meta.

[27] Markku Leino, Alexandra Viel, and Robert E Zillich. "Electronically excited rubidium atom in helium clusters and films. II. Second excited state and absorption spectrum". In: *The Journal of chemical physics* 134 (2011), p. 024316. URL: https://doi.org/10.1063/1.3528936.

[28] Arnau Vilà, Miguel Paniagua, and Miguel González. "Vibrational energy relaxation dynamics of diatomic molecules inside superfluid helium nanodroplets. The case of the I_2 molecule". In: *Physical Chemistry Chemical Physics* 20 (2018), pp. 118–130. DOI: 10.1039/C7CP05694J.

[29] Dominik Pentlehner et al. "Laser-induced adiabatic alignment of molecules dissolved in helium nanodroplets". In: *Physical Review A* 87 (2013), p. 063401. URL: https://doi.org/10.1103/PhysRevA.87.063401.

[30] Lars Christiansen et al. "Alignment enhancement of molecules embedded in helium nanodroplets by multiple laser pulses". In: *Physical Review A* 92 (2015), p. 053415. URL: https://doi.org/10.1103/PhysRevA.92.053415.

[31] Benjamin Shepperson et al. "Observation of rotational revivals for iodine molecules in helium droplets using a near-adiabatic laser pulse". In: *Physical Review A* 97 (2018), p. 013427. URL: https://doi.org/10.1103/PhysRevA.97.013427.

[32] Adam S Chatterley, Benjamin Shepperson, and Henrik Stapelfeldt. "Three-dimensional molecular alignment inside helium nanodroplets". In: *Physical review letters* 119 (2017), p. 073202. URL: https://doi.org/10.1103/PhysRevLett.119.073202.

[33] H Schmidt et al. "Predissociation dynamics of lithium iodide". In: *The Journal of chemical physics* 142 (2015), p. 044303. URL: https://aip.scitation.org/doi/pdf/10.1063/1.4906512.

[34] CP Schulz, P Claas, and F Stienkemeier. "Formation of K* He exciplexes on the surface of helium nanodroplets studied in real time". In: *Physical review letters* 87 (2001), p. 153401. URL: https://doi.org/10.1103/PhysRevLett.87.153401.

[35] F Stienkemeier et al. "Coherence and relaxation in potassium-doped helium droplets studied by femtosecond pump-probe spectroscopy". In: *Physical review letters* 83 (1999), p. 2320. URL: https://doi.org/10.1103/PhysRevLett.83.2320.

[36] C Giese et al. "Formation and relaxation of RbHe exciplexes on He nanodroplets studied by femtosecond pump and picosecond probe spectroscopy". In: *The Journal of chemical physics* 137 (2012), p. 024316. URL: https://doi.org/10.1063/1.4772749.

[37] G Droppelmann et al. "Formation times of RbHe exciplexes on the surface of superfluid versus normal fluid helium nanodroplets". In: *Physical review letters* 93 (2004), p. 023402. URL: https://doi.org/10.1103/PhysRevLett.93.023402.

[38] M Mudrich et al. "Quantum interference spectroscopy of rubidium-helium exciplexes formed on helium nanodroplets". In: *Physical review letters* 100 (2008), p. 023401. URL: https://doi.org/10.1103/PhysRevLett.100.023401.

[39] Andreas Przystawik et al. "Light-induced collapse of metastable magnesium complexes formed in helium nanodroplets". In: *Physical Review A* 78 (2008), p. 021202. URL: https://doi.org/10.1103/PhysRevA.78.021202.

[40] S Göde et al. "Time-resolved studies on the collapse of magnesium atom foam in helium nanodroplets". In: *New Journal of Physics* 15 (2013), p. 015026. URL: http://iopscience.iop.org/article/10.1088/1367-2630/15/1/015026/meta.

[41] MA Douglas, RH Hauge, and JL Margrave. "Electronic adsorption spectra of the Group 3A metal dimers isolated in cryogenic matrixes". In: *The Journal of Physical Chemistry* 87 (1983), pp. 2945–2947. URL: https://pubs.acs.org/doi/pdf/10.1021/j100238a045.

[42] K Balasubramanian and Junqing Li. "Spectroscopic properties and potential energy surfaces of In_2". In: *The Journal of chemical physics* 88 (1988), pp. 4979–4986. URL: https://doi.org/10.1063/1.454677.

[43] Zhou Ling-Song, Yan Bing, and Jin Ming-Xing. "Multireference calculations on low-lying states and the X3Πu- 3Πg absorption spectra of indium dimers". In: *Chinese Physics B* 22 (2013), p. 043102. URL: http://iopscience.iop.org/article/10.1088/1674-1056/22/4/043102/meta.

[44] Sascha Ranftl. "Ultrafast photoinduced ejection dynamics of indium atoms inside superfluid helium nanodroplets". MA thesis. Institute of Experimental physics, Graz University of Technology, 2017.

[45] Stefan Cesnik. "The role of molecular symmetries in non-adiabatic relaxation dynamics". MA thesis. Institute of Experimental physics, Graz University of Technology, 2018.

[46] Bernhard Thaler. "Ultrafast molecular photodissociation dynamics studied with single-pulse femtosecond photoelectron-photoion-coincidence spectroscopy". MA thesis. Institute of Experimental physics, Graz University of Technology, 2017.

[47] Pfeiffer Vacuum. *SingleGauge TPG 261*. Oct. 3, 2018. URL: http://www.idealvac.com/files/brochures/Pfeiffer_Single_Gauge_TPG261.pdf.

[48] Melanie Mucke et al. "Performance of a short "magnetic bottle" electron spectrometer". In: *Review of Scientific Instruments* 83 (2012), p. 063106. URL: https://doi.org/10.1063/1.4729256.

[49] M. Meyer et al. "Femtosecond solvation dynamics of indium dimers inside superfluid helium nanodroplets". In: *EPJ Web of Conferences* (2018). accepted.

[50] B. Thaler et al. "Solvation properties of atoms inside superfluid helium nanodroplets: the borderline case of indium". In: *Physical Chemistry Chemical Physics* (2018). under review.

[51] Evgeniy Loginov, Dominic Rossi, and Marcel Drabbels. "Photoelectron spectroscopy of doped helium nanodroplets". In: *Physical review letters* 95 (2005), p. 163401. URL: https://journals.aps.org/prl/pdf/10.1103/PhysRevLett.95.163401.

[52] Dorothy S Ginter, Marshall L Ginter, and K Keith Innes. "Electronic Spectra of the Ga2, In2, and Tl2 Molecules". In: *The Journal of Physical Chemistry* 69 (1965), pp. 2480–2483. URL: https://pubs.acs.org/doi/pdf/10.1021/j100891a512.

[53] Burkhard Schmidt and Ulf Lorenz. "WavePacket: A Matlab package for numerical quantum dynamics. I: Closed quantum systems and discrete variable representations". In: *Computer Physics Communications* 213 (2017), pp. 223–234. URL: https://doi.org/10.1016/j.cpc.2016.12.007.

[54] Philip M Morse. "Diatomic molecules according to the wave mechanics. II. Vibrational levels". In: *Physical Review* 34 (1929), p. 57.

[55] Jens Peder Dahl and Michael Springborg. "The Morse oscillator in position space, momentum space, and phase space". In: *The Journal of chemical physics* 88 (1988), pp. 4535–4547.

List of Figures

1.1 Schematic scheme of WP excitation and measurement 2
1.2 WP dephasing and dissipation 4
1.3 WP revival 5
1.4 In_2 potential energy curves 7

2.1 Schematic representation of the experimental setup 10
2.2 Schematic circuit diagram 11
2.3 Pin assignment for pressure control [47] 12
2.4 Flow control sensor 13
2.5 Energy resolution of TOF spectrometer 14

3.1 Time evolution of the In_2-He_N system after photoexcitation 17
3.2 Excitation spectrum of In_2 inside He_N 19
3.3 Transient PE spectrum within the first 3 ps and schematic potential energy curves 20
3.4 Transient PE spectra and FT for excitation at 345 nm, 5 mm LBO crystal, 18 K nozzle temperature 22
3.5 SWFT analysis of figure 3.4 23
3.6 Transient PE spectra and FT for excitation at 345 nm, 5 mm LBO crystal, 15 K nozzle temperature 24
3.7 SWFT analysis of figure 3.6 25
3.8 Transient PE spectra and FT for excitation at 345 nm, 1 mm BBO crystal, 15 K nozzle temperature 27
3.9 SWFT analysis of figure 3.8 28
3.10 Compare oscillation contrast 29
3.11 Frequency shift at 345 nm excitation wavelength 29
3.12 Transient PE spectrum and FT for excitation at 333 nm 31
3.13 Integrated electron yield for excitation at 333 nm 31

3.14 FT of higher and lower energetic PE peak for excitation at 333 nm 32
3.15 SWFT analysis of figure 3.12 32
3.16 SWFT analysis of higher energy PE peak in figure 3.12 at excitation with 333 nm 33
3.17 SWFT analysis of lower energy PE peak in figure 3.12 at excitation with 333 nm 34
3.18 Transient PE spectrum and FT for excitation at 327 nm 35
3.19 Transient PE spectrum for excitation at 360 nm 36
3.20 Integrated electron yield for excitation at 360 nm 36
3.21 Transient PE spectrum and FT for excitation at 365 nm 38
3.22 SWFT analysis of figure 3.21 38
3.23 FT at 365 nm excitation wavelength for low and high time delay 39
3.24 Compare transient PE spectra for excitation at 345 nm and 365 nm 40
3.25 Ion yield at large pump-probe time delay for 18 K nozzle temperature . . . 42
3.26 Ion yield at small and large pump-probe time delay for 15 K and 13 K nozzle temperature 42
3.27 Ion yield as a function of pick up current 43
3.28 Transient mass spectrum and integrated In, In-He_n and In_2 yield 44
3.29 Mass spectra at 2 ps and 200 ps time delay for excitation at 345 nm 45
3.30 Pulse energy dependence 45
3.31 Primary oscillation of In-He_n at 345 nm excitation wavelength 46
3.32 SWFT analysis of figure 3.31 47
3.33 No full revival of WP in exciplexes at 345 nm excitation wavelength 48

4.1 Calculated Morse potentials for In_2 50
4.2 B $^3\Pi_g$(II) state with vibrational levels and Gaussian laser pulse profile . . . 51
4.3 Vibrational WPs 53
4.4 Temporal evolution of position operator expectation value 55
4.5 Fractional revivals of the WP 55
4.6 FTs of position operator expectation values 56

6.1 Transient PE spectrum and integrated electron yield 64
6.2 Schematic frequency spectra 64
6.3 FT of transient PE spectrum 65
6.4 Modified PE spectrum obtained by filtering low frequencies 65
6.5 Hamming window function and its FT 66
6.6 Sliding Window Fourier spectrum 67

List of Tables

2.1 TOF Energy Resolution 14

3.1 Pump and probe pulse energies 41

4.1 Morse potential parameters for In_2 50
4.2 WP weight factors 54

6.1 Physical constants and atomic mass of In 69

Listings

6.1 Matlab code for SWFT analysis of transient PE spectra 67
6.2 Matlab code for WP simulation 69

Danksagung

Zum Abschluss meiner Diplomarbeit möchte ich zuallererst den Mitgliedern meiner Forschungsgruppe danken, für all die Dinge, die ich im Laufe meiner Zeit hier beigebracht bekommen habe und lernen konnte.

Ganz besonders bedanke ich mich bei Assoc.Prof. Dipl.-Ing. Dr.techn. Markus Koch für die Möglichkeit halbtags an meiner Diplomarbeit arbeiten zu können. Durch die Diskussionen auf Augenhöhe bekommt man wirklich das Gefühl etwas an der Forschung beitragen zu können. Und danke Markus, dass du mich dazu drängst mein Bestes zu zeigen.

Ein großes Dankeschön gebührt auch Bernhard Thaler, der mich mit viel Geduld in den Forschungsalltag im Femtolabor eingeschult hat und der jederzeit mit Rat und Tat zur Seite steht, egal, worum es geht. Danke für die gemeinsame Zeit im Labor, das Konzipieren der Messreihen und die Hilfe bei der Interpretation der Ergebnisse.

Pascal Heim, du bekommst zwar keine ganze Seite, aber auch dir möchte ich ein großes Dankeschön ausprechen. Danke für die Hilfe bei den Wellenpaketrechnungen, die SWFT Auswertung und ganz besonders bedanke ich mich für den 8 Uhr Kaffee!

Auch möchte ich mich bei Leonhard Treiber für die gemeinsamen Kaffeepausen, den guten Zuspruch und die zahllosen Tipps betreffend LaTeXund das Schreiben der Diplomarbeit bedanken und bei Stefan Cesnik und Werner Kleinsasser für die angehnehme Zeit auf der Uni.

Bei Univ.-Prof. Dipl.-Phys. Dr.rer.nat. Wolfgang E. Ernst möchte ich mich für die Möglichkeit bedanken meine Diplomarbeit hier, am Institut für Experimentalphysik, verfassen zu können.

Auch meiner Familie danke ich von ganzem Herzen für die große Unterstützung und den Rückhalt, den ich während meiner gesamten Studienzeit erfahren habe.

Danke Mama, für alles. Ohne dich wäre ich nie so weit gekommen. Danke Bernhard, dafür, dass du mir immer alles zugetraut hast.

Danke Alice, dass ich immer zu dir aufschauen kann. Danke Alexander, dass du mir zeigst, wie hart man arbeiten kann.

Danke Flo, dass du immer für mich da bist, wenn auch nicht immer örtlich. Und ganz besonders danke für die Zeit, die ich dank dir länger zur Fertigstellung der Diplomarbeit auf der Uni verbringen konnte.

Und danke Mia, dafür, dass du mir jeden Tag Dinge beibringst, die man auf keiner Uni lernen kann.